DESIGN, FABRICATION, AND EXPERIMENTAL CHARACTERIZATION OF A FOCUSABLE SOLAR SIMULATOR FOR HIGH AND LOW FLUX SOLAR THERMAL APPLICATIONS

RAJIV BADALOO

A DISSERTATION SUBMITTED TO
THE FACULTY OF GRADUATE STUDIES
IN PARTIAL FULFILLMENT OF THE REQUIREMENTS
FOR THE DEGREE OF
MASTER OF APPLIED SCIENCE

GRADUATE PROGRAM IN MECHANICAL ENGINEERING
YORK UNIVERSITY
TORONTO, ONTARIO
APRIL 2025

Abstract

High-flux solar simulators (HFSS) advance solar thermal research but are traditionally costly and complex, limiting access for smaller institutions. This thesis presents a low-cost, adaptable solar simulator using commercially available xenon arc cinema searchlights and Fresnel lenses for dynamic irradiance control. The system was characterized through direct flux measurements with a pyranometer and indirect flux mapping via a CMOS camera, enabling detailed analysis of irradiance distribution, temporal stability, and efficiency. Experimental results showed an average irradiance of 2819 W/m² over a 12×12-inch area, peak irradiance of 2348 kW/m² with Fresnel lens concentration, and efficiencies up to 22.4% at full intensity. Real-world tests on radiative cooling coatings confirmed the simulator's capability to replicate concentrated solar conditions accurately. This study demonstrates a scalable, practical alternative to traditional HFSS, enhancing accessibility for smaller research facilities and laying a foundation for future multi-lamp and advanced optical configurations.

Acknowledgements

This thesis would not have been possible without the support, encouragement, and belief of some incredible people in my life.

First and foremost, I want to thank my parents, Munair Badaloo and Anna Henry, for always being in my corner. Their unwavering support, love, and sacrifices have shaped the person I am today. No matter what path I chose, they backed me without hesitation, and for that, I am forever grateful.

A special and heartfelt thank you to my great-grand-uncle, Noel Singh. He was the one who first planted the idea of engineering in my mind and pushed me to pursue it when I was not even sure of it myself. His guidance did not stop at my undergrad—he kept pushing me to go further, to challenge myself, and to pursue this Master's. His recent passing has left a huge void, but I carry his lessons and encouragement with me every day. This thesis is, in many ways, a result of his belief in me, and I hope it makes him proud.

I also want to express my gratitude to my supervisor, Professor Thomas Cooper. His guidance, patience, and expertise have been invaluable throughout this research. His insights and support helped shape not only this thesis but also the way I approach problem-solving and engineering as a whole.

To my friends, colleagues, and everyone who has been part of this journey—thank you. Whether it was offering advice, listening to me rant about experiments, or just being there for a much-needed break, your support has meant the world to me.

This thesis is dedicated to all of you. I couldn't have done it without you.

Contents

List of Tables

List of figures

Nomenclature

HFSS – high flux solar simulator

CMOS – complimentary metal-oxide semiconductor

h_i – Initial lamp height

gv – gray value, (Digital number)

RMS – Root mean square

NRMS – Normalized root mean square

CF – Calibration factor

E_{pyra} – Irradiance measured by the pyranometer

Δt_{cali} – Exposure time of calibration image

$\Delta t_{fluxmap}$ – Exposure time of a given image

ROI – Region of interest

gv_{ROI} – Average Grey value at the ROI

$T_{measured}$ – Measured temperature

T_{actual} – Actual temperature calculated

U – Uncertainty

ε – emissivity

α – Absorptivity

σ – Stephan- Boltzmann Constant

1. Introduction

1.1 Thesis outline

Chapter 1: Introduction

This chapter introduces the motivation and scope of the research by highlighting the need for an accessible, focusable high-flux solar simulator (HFSS). It explains how conventional HFSS systems can be costly and complex, particularly for smaller institutions. The chapter then outlines the central objective of developing a cost-effective solar simulator using a commercial xenon arc cinema searchlight, capable of producing both high- and low-flux conditions.

Chapter 2: Background and Theory

This chapter provides a detailed review of the principles underlying solar simulators, concentrating optics, and flux mapping techniques. It includes an overview of high-flux solar simulators, their applications, and the advantages of using xenon arc searchlights for solar thermal research. Additionally, theoretical models for flux concentration, temporal instability, and optical efficiency are discussed.

Chapter 3: Experimental Setup

This chapter details the experimental apparatus, including the xenon arc searchlight, optical table, pyranometer, CMOS camera, Lambertian target, and Fresnel lens. The setup is designed to facilitate direct and indirect flux mapping, power measurement, and efficiency analysis. The integration of height-adjustable components for focusability is also described.

Chapter 4: Methodology

The methodology chapter outlines the experimental procedures for characterizing the solar simulator. It includes details on flux measurement techniques using both pyranometer and CMOS camera, calibration processes, perspective correction, and data processing methods. Additionally, this chapter describes how power output, flux distribution, and system efficiency are determined.

Chapter 5: Results

The results chapter presents the key findings from the experimental characterization. It includes flux maps, efficiency calculations, and an evaluation of the searchlight's performance under

different configurations. Comparisons between direct and indirect flux mapping methods, as well as an assessment of temporal stability and non-uniformity, are included.

Chapter 6: Exemplary Demonstration

This chapter showcases an application of the solar simulator in a practical experimental scenario. It includes a separate background, methodology, results, and discussion for a case study demonstrating the simulator's ability to test materials such as radiative cooling coatings under controlled high-flux conditions.

Chapter 7: Conclusion

This chapter summarizes the research findings, discusses the significance of the results, and outlines potential improvements for future work. It includes recommendations for enhancing the simulator's performance, integrating additional optical components, and expanding its application to multi-lamp configuration.

1.2 Literature review

High-flux solar simulators (HFSS) are crucial in concentrated solar thermal research, providing stable, high-intensity radiation under repeatable conditions (Ekman et al., 2015; Gallo et al., 2017; Sarwar et al., 2014). Unlike natural sunlight, which can vary and be intermittent, HFSS enable consistent experimental environments vital for advancing solar thermal systems, thermochemical reactors, and concentrated photovoltaic (CPV) technologies.

Early solar simulators relied on tungsten-halogen and xenon lamps for basic thermal tests (Ekman et al., 2015). Modern designs predominantly use xenon arc lamps because of their broad, continuous emission spectra—closely matching the solar spectrum—and their ability to provide intense, stable radiation (Krueger et al., 2011; Petrasch et al., 2007). Despite higher costs and more complex cooling needs, xenon arc lamps remain the standard choice for reliable and accurate solar simulation (Ekman et al., 2015; Krueger et al., 2011; Sarwar et al., 2014).

Various optical configurations have been developed for concentrating solar radiation in HFSS setups. Ellipsoidal reflectors, due to their excellent optical performance and ease of integration with xenon lamps, have been widely adopted in many research facilities (Gill et al., 2015; Petrasch et al., 2007). However, alternative optical designs such as Fresnel lenses have gained attention for their potential cost-effectiveness and reduced complexity. For instance, Wang et al. (2017) demonstrated a Fresnel lens-based HFSS achieving high flux levels with significantly lower costs compared to traditional ellipsoidal reflector setups. Such developments illustrate the ongoing effort to improve efficiency, reduce costs, and enhance the accessibility of HFSS technology.

Measurement techniques for characterizing the radiation output of HFSS are critical for ensuring accurate experimental conditions. Flux mapping methods, which measure and visualize spatial radiation distribution, are widely utilized. Direct measurement techniques typically involve sensors placed directly at the focal plane, but these methods often face challenges due to spatial resolution limitations and complexity (Xiao et al., 2019). Consequently, indirect flux mapping methods, involving Lambertian targets and CCD cameras, have been developed and refined, offering higher resolution and more comprehensive characterization of the flux distribution (Xiao et al., 2019; Dai et al., 2019). Recent improvements, such as dual Lambertian target systems, have further enhanced the accuracy and reliability of indirect methods by eliminating interpolation errors (Xiao et al., 2019).

Several notable HFSS systems have been reported in the literature. A 130 kWe HFSS, employing 13 xenon lamps, achieved ultra-high fluxes exceeding 11 MW/m², demonstrating significant advancements in optical concentration and flux uniformity (Zhu et al., 2020). Another innovative design involved a 10 kWe HFSS characterized by Abuseada et al. (2019), utilizing a single xenon arc lamp and detailed flux mapping techniques, which confirmed its capability to achieve flux levels around 6990 kW/m², highlighting the effectiveness of optimized optical design and advanced characterization methods.

In summary, high-flux solar simulators have evolved significantly, driven by advances in optical design, flux measurement methodologies, and cost-effective configurations. The continued development and refinement of HFSS technologies remain vital for advancing concentrated solar thermal research, providing critical infrastructure for the exploration of innovative solar energy solutions.

1.2 Motivation

This research originated from the goal of converting Martian regolith into oxygen and structural metals using concentrated sunlight. Achieving such in-situ resource utilization requires a solar simulator capable of replicating Martian conditions and delivering the high fluxes needed for these conversion processes. However, commercial systems meeting these demands are typically large, complex, and prohibitively expensive. From the, the focus of the work shifted to developing a low-cost solar simulator that can still achieve the high flux necessary for these types of solar thermal applications.

1.3 Goals and Objectives

The primary goal of this research is to develop and characterize a low-cost, high-flux solar simulator utilizing commercial cinema searchlight technology for solar thermal applications. This study aims to provide an alternative to conventional high-flux solar simulators (HFSS), which are often expensive and complex, thereby making advanced solar research more accessible to smaller research institutions and industry stakeholders. The successful realization of this objective will facilitate the development of high-flux testing environments for various solar thermal applications, including material testing and energy conversion efficiency studies.

Objective 1: Construct an experimental setup using a commercial cinema xenon searchlight with condensing optics capable of achieving high flux.

The experimental set up will include cinema searchlight with integrated condensing optics to achieve high flux densities. This involves incorporating optical components such as Fresnel lenses to enhance light concentration and implementing a motorized adjustable frame to enable precise height and positional adjustments for optimal focusing.

Objective 2: Develop and implement flux characterization methods to evaluate the simulator's performance through efficiency, temporal stability, and flux distribution measurements.

These techniques will characterize the simulator's performance in terms of efficiency, temporal stability, and flux distribution. Direct and indirect flux mapping methods will be employed using a pyranometer and a CMOS camera to assess irradiance distribution and intensity. The optical-to-electrical efficiency of the simulator will be quantified by correlating the power input of the xenon

lamp to the total measured irradiance output. Additionally, spatial and temporal flux stability will be analyzed to ensure the system's reliability and repeatability.

Objective 3: Demonstrate the simulator's real-world applicability through a representative evaluation.

This will be achieved by collaborating with an industry partner to test state-of-the-art radiative cooling coatings under simulated sunlight. The coatings will be evaluated for their cooling efficiency, durability, and degradation over time. The results will determine the feasibility of these coatings for practical applications and validate the effectiveness of the simulator for material testing under controlled high-flux conditions.

By achieving these objectives, this research will establish a cost-effective, capable solar simulator as a viable alternative to traditional HFSS systems. The study will broaden accessibility to concentrated solar research and contribute to advancements in solar thermal and photovoltaic applications.

2. Background and Theory

2.1 Introduction

High-flux solar simulators (HFSS) play a crucial role in solar thermal research by providing a controlled laboratory environment to evaluate concentrated solar power (CSP) technologies, solar thermochemical reactions, and material performance under high irradiance conditions [1]. Unlike natural sunlight, which fluctuates due to atmospheric conditions and time of day, HFSS provide stable and repeatable illumination, enabling controlled experimental environments [1]. By eliminating these environmental variables, HFSS allow researchers to isolate and study the impact of solar radiation under consistent conditions, improving the accuracy and reliability of experimental results [3].

The primary function of an HFSS is to replicate the spectral and intensity characteristics of natural sunlight while achieving the high flux densities required for concentrated solar applications [2]. These systems typically use high-intensity light sources, such as xenon arc lamps, in combination with optical components like Fresnel lenses and ellipsoidal reflectors to generate collimated or concentrated beams [4]. This design allows for effective testing of solar receivers, reactors, and photovoltaic devices under controlled and reproducible conditions.

This chapter explores the fundamental principles of HFSS, including the role of xenon arc lamps, their spectral characteristics, and the significance of condensing optics such as Fresnel lens and parabolic mirrors. Additionally, different flux measurement techniques, including pyranometer-based direct measurements and indirect flux mapping using CMOS cameras, are discussed to provide insight into experimental validation methods. These foundational concepts establish the framework for understanding the theoretical principles and experimental methodologies used in high-flux solar simulation research.

2.2 High-Flux Solar Simulators

The fundamental principles governing HFSS operation include spectral match, flux concentration, temporal stability, and spatial uniformity. Each of these principles is critical to ensuring that the simulator produces results comparable to real-world solar applications.

Spectral Match: The ability of the simulator to closely replicate the Air Mass 1.5 (AM1.5) solar spectrum is crucial for experiments that require an accurate reproduction of real-world solar conditions. Xenon arc lamps are commonly used due to their broad spectral output, but spectral filters are often required to refine the output to better match the solar spectrum[1]. The deviation of the spectral output from natural sunlight can lead to errors in photovoltaic testing and solar thermal efficiency measurements. Advances in optical filtering technologies, including dichroic and absorption filters, help refine the spectral match, improving the fidelity of experimental conditions.

Flux Concentration: HFSS utilize high-intensity discharge lamps, such as xenon arc lamps, in conjunction with condensing optics like Fresnel lenses and ellipsoidal reflectors to achieve high flux densities [4]. These optical elements focus light onto a small target area, simulating the concentration effects observed in real concentrated solar powered (CSP) systems. The flux concentration can be adjusted based on the specific needs of an experiment, allowing for variation in temperature profiles and heat flux distributions across test materials.

Temporal Stability: Unlike natural sunlight, HFSS provide consistent irradiance over time, which is critical for long-duration experiments. Power regulation and active feedback control systems help mitigate fluctuations. Instability in irradiance can introduce inconsistencies in experimental results, particularly in thermal degradation studies and long-duration solar reactor performance assessments. Advanced power supply units with real-time monitoring and correction capabilities ensure that the output remains stable throughout the duration of the experiment [8].

Spatial Uniformity: Ensuring an even distribution of flux over the target area is essential for minimizing measurement errors and ensuring reproducibility in material testing. Lambertian targets and indirect flux mapping techniques assist in evaluating and improving uniformity [5]. Uneven flux distribution can lead to localized overheating in materials, skewing results in thermal stress and degradation studies. Modern HFSS designs incorporate homogenizing optics and multi-

lamp configurations to reduce spatial variations and improve uniformity across the testing surface [1].

Furthermore, innovations in HFSS technology continue to improve system performance. Computational modeling techniques, such as Monte Carlo ray tracing, allow researchers to predict and optimize flux distributions before physical implementation [9].

By understanding these principles, researchers can design and optimize HFSS configurations to meet the specific requirements of various solar energy applications.

2.3 Xenon Arc Lamps as HFSS Sources

Xenon arc lamps function by sustaining a high-intensity discharge between tungsten electrodes in a high-pressure xenon environment, creating a plasma that emits a broad-spectrum output closely resembling blackbody radiation [1,10]. This includes ultraviolet light (200–400 nm), which contributes to photochemical processes and material degradation studies; visible wavelengths (400–700 nm), aligning well with natural daylight for photovoltaic testing; and infrared radiation (>700 nm), providing thermal energy crucial for solar thermal applications. Their short-arc design minimizes light dispersion, allowing a high portion of emitted radiation to form a well-defined beam—an important characteristic for high-flux solar simulator (HFSS) setups requiring controlled, intense illumination. Furthermore, xenon arc lamps' compact size, high brightness, and comprehensive spectral coverage make them suitable for CSP research, photovoltaic characterization, and material testing [4]. Where greater spectral fidelity is needed, optical filters can reduce emission peaks and more closely match the AM1.5 solar spectrum [4]. Figure 2.1 compares the xenon arc lamp's spectral distribution with the ASTM standard AM1.5 natural solar irradiation (Gueymard et al., 2002).

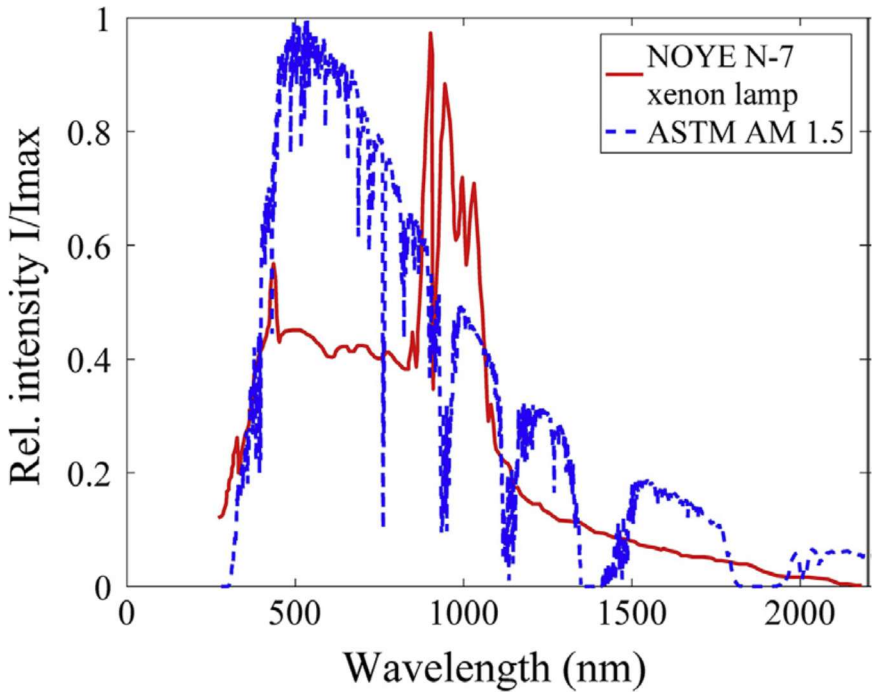

Figure 2.1: Comparison of the spectral distribution of Xenon lamp and ASTM standard AM 1.5 natural solar irradiation (Gueymard et al., 2002).

2.3.1 Advantages of Xenon Arc Lamps in HFSS

The use of xenon arc lamps in HFSS offers several advantages. These lamps emit radiation across a wide range of wavelengths. Their high flux output can achieve intensities exceeding 10 MW/m², making them suitable for CSP and high-temperature material testing [4]. The steady output of xenon arc lamps ensures consistency in long-duration experiments, reducing measurement uncertainties. Additionally, their compact arc size allows for efficient optical collection and focusing, facilitating integration with optical elements such as ellipsoidal reflectors and Fresnel lenses [3].

Another major advantage of xenon arc lamps is their rapid start-up time and ability to reach full intensity within seconds. This allows for efficient experimentation without significant warm-up delays. Unlike other high-intensity discharge lamps, xenon lamps do not require a long stabilization period, making them ideal for experiments requiring frequent on-off cycling [1].

The durability of xenon arc lamps is another advantage, with many lamps having lifetimes exceeding 1000 hours under controlled operating conditions. However, proper maintenance and monitoring of electrical input parameters are necessary to maximize their lifespan. Regular calibration of the optical system, along with appropriate cooling mechanisms, helps maintain consistent performance throughout the lamp's operational lifetime [11].

2.3.2 Challenges and Limitations

Despite their advantages, xenon arc lamps also present significant challenges and limitations. Firstly, these lamps require substantial electrical input and robust cooling mechanisms, typically involving either air cooling for lower wattage xenon lamps or water-cooling systems for higher-powered lamps. Forced-air cooling is also commonly applied to manage heat dissipation from reflectors and lamp housings, preventing overheating and damage [1][4]. The high electrical power demand necessitates specialized power supplies capable of delivering stable and precise electrical currents, as fluctuations can impact the reproducibility of experimental results [2][10].

Another notable limitation is the spectral mismatch. Although xenon arc lamps produce a broad emission spectrum closely resembling natural sunlight, they exhibit intense emission peaks, notably at wavelengths around 800-1000 nm in the near-infrared (NIR) region and around 350-450 nm in the ultraviolet (UV) region [3]. These peaks significantly deviate from the standard solar spectrum, potentially leading to inaccuracies in photovoltaic efficiency tests and thermochemical reaction analyses. Implementing optical filters can address these deviations but at the cost of reducing overall irradiance intensity [3].

Xenon lamps also pose significant safety risks due to the high pressures (up to 40 bar), posing significant security risks such as the potential for lamp explosions, especially when multiple lamps are operated in arrays. For instance, the University of Adelaide highlighted safety concerns regarding the vulnerability of xenon arc bulbs to explosions, particularly in multi-lamp configurations where a single bulb explosion could trigger cascading failures, increasing both safety risks and operational downtime [11]. The risk of lamp explosion demands careful handling and strict adherence to safety protocols. This factor, coupled with their high cost and the need for complex and expensive power supply systems, contributes to operational and financial challenges [11].

Electrode degradation is another inherent challenge, resulting in a gradual reduction of lamp efficiency over time. Tungsten electrode erosion necessitates frequent replacements, increasing both maintenance efforts and operational costs. Typical lamp lifetimes can range from 600 to over 1000 hours, dependent on the careful management of cooling conditions and operating currents recommended by manufacturers [11].

The intense thermal loads produced by xenon arc lamps further highlight the necessity of effective cooling strategies. Inadequate cooling accelerates electrode degradation; risks damage to reflector coatings and significantly reduces lamp efficiency and lifespan. Therefore, incorporating comprehensive and efficient cooling solutions into HFSS design is crucial for sustaining reliable performance during extended operational periods [1].

2.4 Experimental Applications

High-flux solar simulators are used in a wide range of research fields including; concentrated solar power (CSP), thermochemical fuel production, high-temperature material testing, and advanced hybrid applications. [1,3,6].

Their capability to simulate high flux levels facilitates the testing and optimization of solar receivers and heat exchangers for CSP technologies, improving energy capture efficiency and thermal durability [10,13]. HFSS also play a significant role in solar thermochemical processes, such as hydrogen generation via water-splitting or redox cycles, where uniform and sustained high temperatures are critical for accurate kinetic evaluation and reactor design [5,15]. For high-temperature materials, HFSS replicate the severe thermal and radiative loads found in CSP and aerospace systems, enabling researchers to examine ceramic coatings, refractory metals, and composite structures for emissivity, thermal expansion, and degradation mechanisms.

Beyond conventional solar energy applications, HFSS are increasingly utilized in hybrid solar-electric systems, from combined photovoltaics-thermoelectric to CSP-PV hybrids, as well as for integrating solar with phase-change materials. Their controlled irradiation assists in optimizing power conversion and thermal management strategies [1]. HFSS further benefit industrial processes like additive manufacturing, allowing non-contact, localized high-flux heating for rapid material processing of advanced alloys and composites [3].

2.5 Optical Components

HFSS High-flux solar simulators (HFSS) utilize precisely arranged optical elements to shape and direct light. Fresnel lenses, ellipsoidal reflectors, collimating mirrors, and diffusers each contribute to achieving target flux distributions, preserving spectral fidelity, and ensuring uniformity. The careful selection and configuration of these optics directly affect overall performance and efficiency in HFSS systems [5]

2.5.1 Fresnel Lens and Its Optical Properties

Fresnel lenses are widely employed in high-flux solar simulators (HFSS) to concentrate light efficiently in a compact form. Unlike traditional convex lenses, they replace a thick curved surface with concentric grooves molded into acrylic or polycarbonate, significantly reducing weight and material while maintaining good optical clarity and durability [6]. As illustrated in Figure 2.2, the grooves refract parallel rays toward a single focal point, achieving high flux concentration essential for solar thermochemical reactions and concentrated photovoltaics. The focal length is determined by the lens's groove structure, which can be optimized for specific irradiance needs [9].

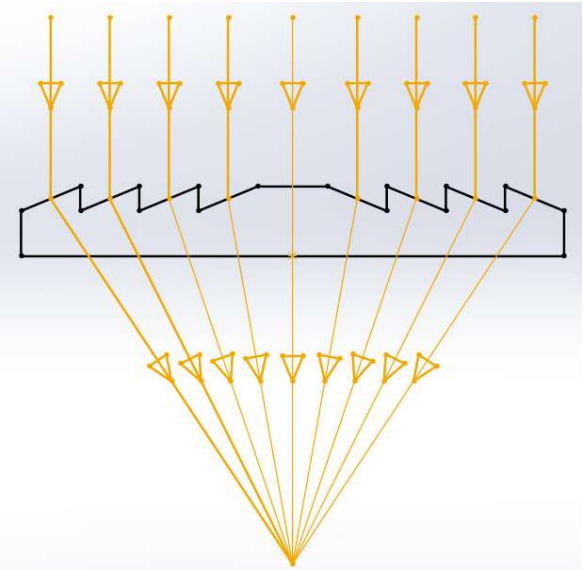

Figure 2.2: Schematic representation basic function of a Fresnel lens. Parallel light rays (yellow) are focused by the concentric sections of the Fresnel lens (black), converging at a single focal point below the lens.

Despite these advantages, Fresnel lenses can exhibit chromatic aberration and diffraction losses, which may create non-uniform flux distributions. To mitigate these effects, secondary optical elements (e.g., homogenizers or secondary reflectors) often accompany Fresnel lenses, improving flux uniformity and minimizing spectral distortions [14]. Ongoing advances in multi-layered, high-precision Fresnel lens technology further enhance optical efficiency and durability, making them a pivotal component in modern HFSS [10].

2.6.2 Parabolic Reflector

Parabolic reflectors are another type of condensing optics used for collimating and redirecting light. As shown in Figure 2.3, parallel incident rays are reflected and focused at a single focal point. Conversely, placing a point source at this focal point produces a nearly collimated beam, an approach that proves valuable for uniform illumination and controlled beam direction in HFSS.

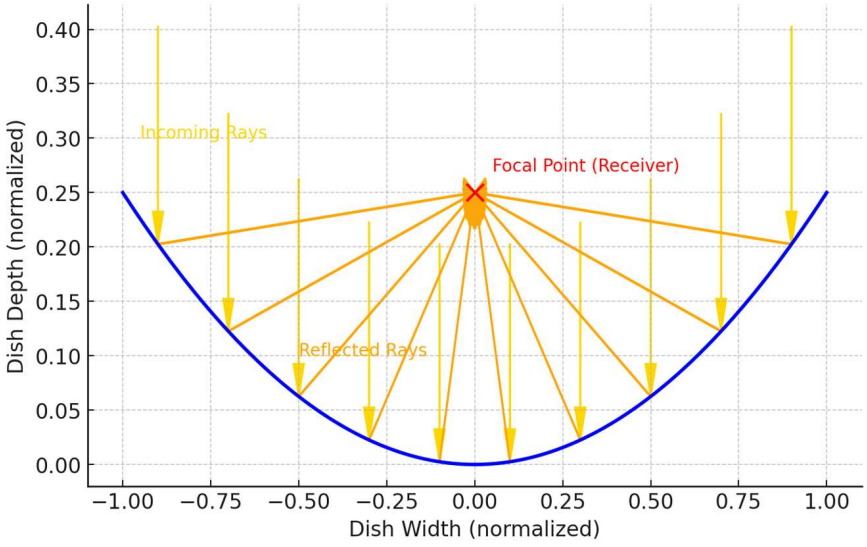

Figure 2.3: Schematic of a Parabolic Dish Reflector: Incoming solar rays (gold) are reflected (orange) toward the focal point (red).

Typically fabricated with aluminum or silver coatings to maximize reflectivity, parabolic reflectors can deliver high-intensity, well-directed flux, crucial in concentrated solar power research and thermal processing. However, their performance may be hindered by surface defects or misalignment, which can generate aberrations or uneven flux distributions. Proper manufacturing tolerances and careful mounting help ensure optimal beam quality [3].

2.6 Flux Measurement Techniques

Measuring solar flux accurately is vital for gauging performance and efficiency in high-flux solar simulators. Because the concentrated radiation in these systems can reach extreme intensities, reliable measurement methods are critical to understand optical layouts, power distributions, and thermal behavior.

Two primary measurement techniques are widely employed:

2.6.1 Pyranometer – Direct mapping

Pyranometers measure solar irradiance (W/m^2) via a thermopile detector that outputs a voltage proportional to the temperature difference between a blackened absorbing surface and a reference. These instruments provide absolute flux values and are widely used in solar research for calibration and validation, owing to their robustness. In high-flux simulators, pyranometers are placed at various points on a grid to map the flux distribution. However, they are limited to low spatial resolution, since each reading represents only one point.

2.6.2 Indirect Flux Mapping with a CMOS Camera

In contrast to pyranometer-based methods, indirect flux mapping employs a CMOS (Complementary Metal-Oxide-Semiconductor) camera in conjunction with a Lambertian target to capture and reconstruct the flux distribution over an extended area. This technique relies on the assumption that grayscale intensity variations in the captured images correlate directly with the incident radiative flux. By calibrating the grayscale response using reference measurements, it is possible to obtain high-resolution flux maps that provide valuable insights into the spatial characteristics of the radiation field.

The standard procedure for CMOS-based flux mapping begins with capturing a reference measurement using a pyranometer or heat flux sensor placed on the Lambertian target. Once a conversion factor between grayscale intensity and absolute flux is established, the pyranometer is removed, and the solar simulator is adjusted to ensure optimal alignment with the target. The camera then captures multiple grayscale images, which are averaged to minimize noise and enhance measurement precision. To further refine the results, perspective correction algorithms are applied to account for geometric distortions caused by camera positioning or lens aberrations [3,4].

One of the primary advantages of CMOS-based flux mapping is its exceptional spatial resolution, enabling the detection of flux non-uniformities, hot spots, and peak intensities that might be missed in discrete-point measurements. Moreover, the method is significantly faster than pyranometer scanning, as a single image captures the entire flux distribution in real time. However, the technique is not without limitations. CMOS sensors require careful calibration to ensure that grayscale variations accurately reflect radiative flux levels. Furthermore, exposure settings, ambient lighting conditions, and camera sensitivity must be carefully controlled to avoid measurement artifacts.

Despite these challenges, indirect flux mapping has become a widely adopted approach in high-flux solar research, particularly for applications where high-resolution spatial characterization is required. The ability to visualize flux distributions in detail makes it an invaluable tool for optimizing simulator performance, refining optical configurations, and assessing the effectiveness of secondary concentrators.

2.6.3 Lambertian Target

A Lambertian surface scatters incident radiation uniformly in all directions, ensuring that reflected intensity remains independent of the observer's angle. This property is essential for indirect flux mapping in high-flux solar simulators. By using CMOS cameras to image the illuminated Lambertian target, the grayscale intensity at each pixel can be correlated with the local flux distribution [5,6,16].

Lambert's cosine law shown in equation 1 states that reflected intensity is proportional to the cosine of the angle between the surface normal and the observation direction:

$$I(\theta) = I_0 \cos(\theta) \qquad \text{(eqn.1)}$$

where I_0 is the intensity under normal incidence. This relationship helps the camera record a radiance unaffected by viewing angle, making flux mapping straightforward. Consequently, Lambertian targets are indispensable for assessing flux distributions in high-temperature solar research [5].

In practical applications Lambertian targets are typically placed at a solar simulator's focal plane to serve as a reference for flux measurements. A camera captures the reflected image, and a heat flux sensor or pyranometer reading provides a reference to calibrate the grayscale intensities [6].

Because they need to maintain high reflectance across ultraviolet, visible, and near-infrared wavelengths, target materials often include ceramic coatings, alumina surfaces, or high-temperature oxide coatings, which allow minimal absorption losses and withstand extended exposure to intense radiation [8,5].

Compared to direct flux measurements, Lambertian targets allow quick, non-intrusive, full-field flux mapping, making them ideal for capturing high-resolution data without scanning multiple points [5]. Nonetheless, their reflectance can drift over time, mandating regular checks and possible recoating to maintain uniform properties. Achieving consistent alignment and uniform illumination can also be challenging in practice [6,8]. Finally, since Lambertian targets only provide indirect flux data through grayscale imaging, all intensities must be post-processed against a reference sensor to yield absolute flux values.

3. Experimental Setup

This study employs direct and indirect flux mapping techniques to evaluate the performance of a commercially available 1 kW xenon arc cinema searchlight, as an affordable solar simulator. The experimental setup consists of a modular optical system designed for precise flux measurements, ensuring accurate data collection for comparative analysis. Figure 3.1 Shows the complete setup of the system.

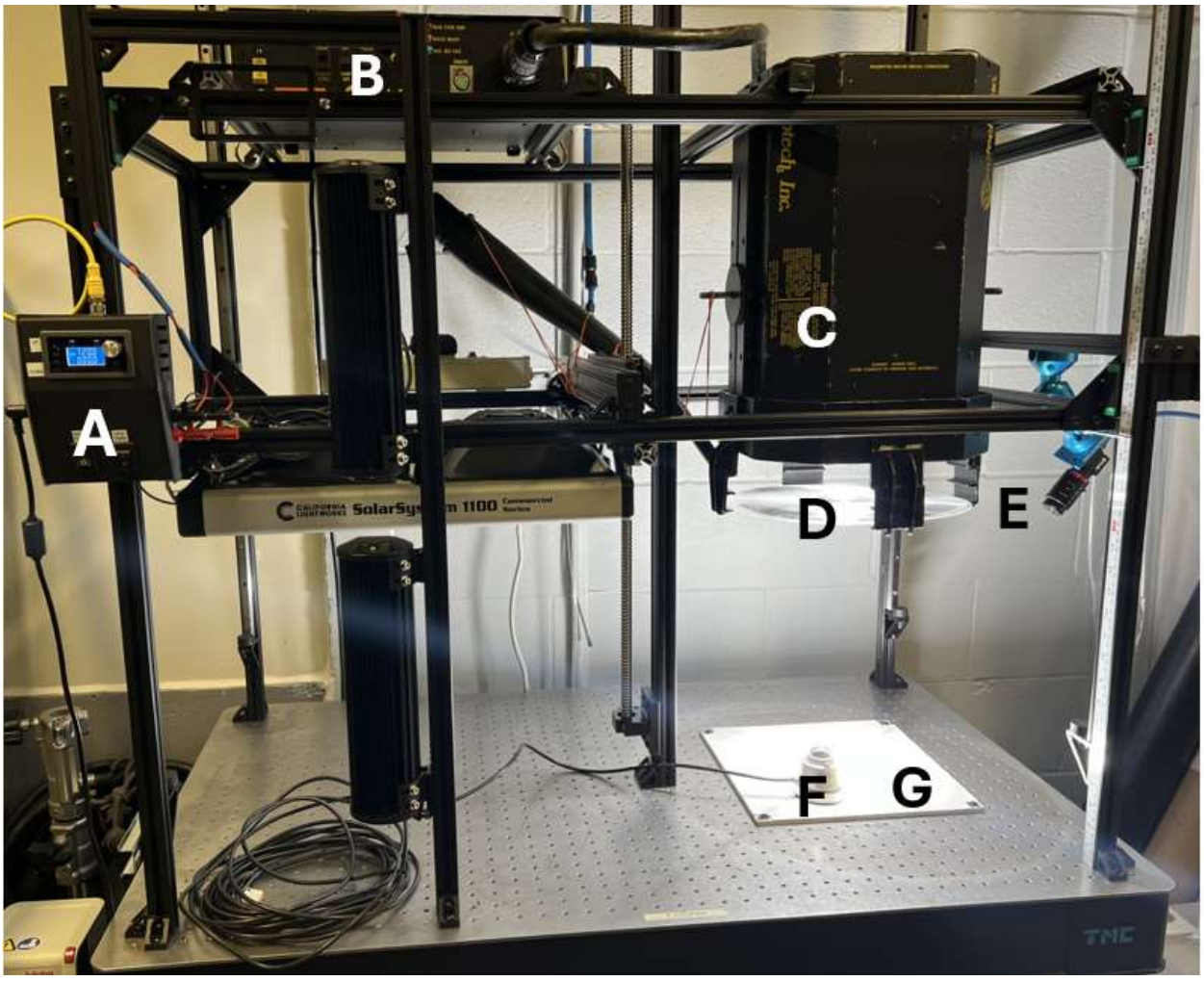

Figure 3.1: Experimental setup for the solar simulator. Components: (A) motor controller for height positioning, (B) power supply for the xenon lamp, (C) commercial xenon arc lamp, (D) Fresnel lens for light focusing, (E) CMOS camera for flux measurement, (F) pyranometer for flux measurement, (G) Lambertian target for producing diffuse reflection of incoming light.

3.1 Optical Table and Frame

The experimental setup is built on a 47 × 29-inch aluminum optical table featuring standard ¼ - 20 threaded hole grid with 1-inch spacing, allowing for precise component alignment. The table sits on an air suspension system that isolates the components on it from external disturbances. Standard 80 - 20 T-slotted framing rails were used to construct an aluminum frame to facilitate the setup. A 6-ft tall frame was created with a rigid box frame for mounting the lamp. An electric motor, coupled with a high ratio gearbox was used to drive a lead screw to allow a 4.5-ft vertical travel range to accommodate different lamp heights. The motorized ball screw system allows for precise vertical positioning of the lamp, with 1 mm accuracy over the 4.5-ft range. A stick-on ruler provides a visual reference for height adjustments. This electronic control (Fig. 3.1A) ensures easy, accurate, repeatable configuration of different lamp positioning. The ability to fine-tune the height facilitates improved control over focal spot size and thus flux distribution.

3.2 Xenon Arc Lamp & Power Supply

The study utilizes a Xenotech Inc. Brightlight 57K, BL571H xenon arc lamp (Fig. 3.1C), powered by a Xenotech Inc. Xenon 1K Ballast, BL571EB power supply (Fig.1B). This 1 kW lamp emits a spectrum similar to natural sunlight, making it ideal for solar simulation. The lamp housing contains ellipsoidal reflectors and internal mirrors designed to collimate the beam, aiming to achieve a more uniform and concentrated illumination across the target. The system has two power settings: 1137W (high-power mode) and 628W (low-power mode). The system also includes built-in cooling fans to maintain stability by dissipating heat efficiently, preventing fluctuations in the lamp's output. The ability to operate at different power settings allows for comparative analysis of flux intensities under varied conditions.

3.3 Flux Measurement Instruments

Flux measurements are obtained using a Kipp & Zonen CM4 pyranometer (Fig. 3.1F) with has a sensitivity of 9.22×10^{-6} V/(W/m²) and a Flir Blackfly S BFS-PGE-31S4M CMOS camera (Fig. 3.1E). The CMOS camera features a 3.2 MP Sony IMX265 sensor, global shutter, and 12-bit resolution, providing high-precision image capture capabilities. Due to the pyranometer's upper limit of 4 suns, it is primarily used for low- and moderate-flux measurements and to properly calibrate the images taken by the CMOS camera, whereas the CMOS camera is employed for low

to high-flux measurements. The combination of both instruments allows for a comprehensive analysis of flux distribution under different operating conditions.

3.4 Lambertian Target

The Lambertian target (Fig. 3.1G) is made from anodized aluminum coated with WhiteOptics's White 98 Film, offering 97.5 ± 0.8% diffuse reflectance (at 550 nm). To preserve its optical properties, a plexiglass and aluminum protective cover was constructed for protecting the target when not in use. The target design is optimized to minimize distortions and enhance measurement accuracy.

3.5 Condensing Optics: Fresnel Lens

A 12-inch diameter Fresnel lens (Fig 3.1D) with a focal length of 8.4 inches is used to concentrate the collimated beam, enhancing local irradiance. The lens enables greater precision in achieving high flux intensities; integration of a Fresnel lens allows for a detailed study of how focused light affects the irradiance profile across the target surface.

To ensure stability and prevent thermal degradation, a custom cooling rig was fabricated to securely hold and actively cool the Fresnel lens shown in Fig. 3.2. The rig consists of two aluminum plates that sandwich the lens, providing structural support while minimizing mechanical stress. An air-cooling system is integrated, featuring an air hose running around the perimeter with eight air jets directed onto the lens surface to dissipate heat efficiently.

Figure 3.2: Cooling rig for Fresnel lens

4. Methodology

The methodology outlines the structured approach used to acquire, process, and analyze flux mapping data, ensuring reproducibility, precision, and thorough evaluation of the xenon arc searchlight's performance as a solar simulator. This section details the experimental procedures, measurement techniques, and analysis methodologies, providing a comprehensive framework for future modifications and optimizations.

4.1 Preliminary Setup

Before initiating data collection, the xenon lamp is carefully positioned at a comfortable working height. The power setting is adjusted to either low or high mode, depending on the experiment's objectives. To ensure stability in lamp output, the system is preheated for 30 minutes, allowing the lamp to reach a thermal equilibrium state. This step minimizes output fluctuations, ensuring consistent measurements across different trials.

Measurements are systematically recorded using the pyranometer for low-to-moderate flux levels and the CMOS camera for both low and high-flux measurements. Given the pyranometer’s upper

limit of 4 suns, only the CMOS camera is employed in all scenarios, enabling comprehensive flux characterization across a broad range of intensities.

4.2 Flux Mapping with Pyranometer

A 12 × 12-inch grid facilitates structured flux measurement, with the pyranometer moved in 1-inch increments to capture 144 data points per cycle. To mitigate short-term fluctuations in lamp output, each measurement is repeated and averaged. Voltage readings from a multi-meter are converted to irradiance using the pyranometer's sensitivity calibration. As a test, the lamp was raised and lowered at select points to assess variation. The irradiance remained consistent, indicating well-collimated light. Figure 4.1 illustrates the optical table with pyranometer measurement positions. The black square represents the 12 × 12-inch target area, while the red circles denote the pyranometer's 1.25-inch diameter sensing region at each measurement point. The grid aligns with the 1-inch hole spacing of the optical table, enabling flux measurements at 144 discrete locations for structured flux mapping. Notably, small gaps remain between the diagonal intersections of adjacent sensing regions, resulting in minor areas that are not directly measured.

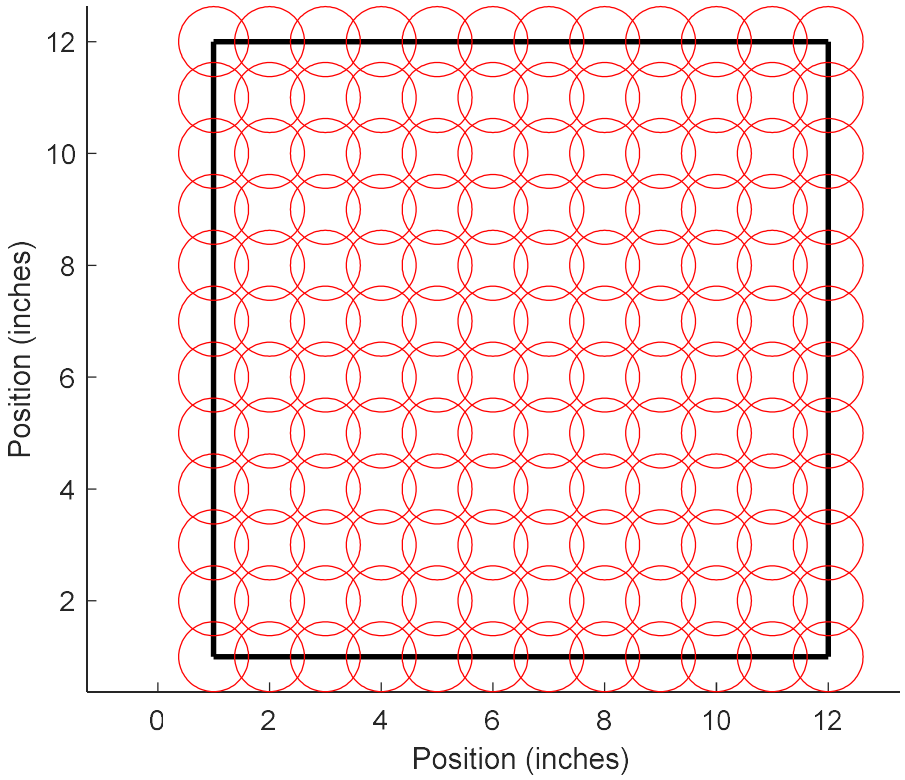

Figure 4.1 : Visualization of the optical table with pyranometer measurement positions. The black square represents the 12 × 12-inch target area, while the red circles indicate the pyranometer's sensing regions at each measurement point. The grid follows a 1-inch step size, capturing flux data at 144 discrete locations for structured flux mapping.

4.3 Flux Mapping with CMOS Camera

To accurately map the flux distribution, the CMOS camera first captures a reference image with the pyranometer in position, the ellipse draw(red) is drawn around the instruments sensor, the region of interest (ROI). The pyranometer is then removed, and the lamp is adjusted by an offset height (*dz*) to ensure direct flux projection onto the Lambertian target while maintaining spatial consistency between measurements, this also caused a change in focus. This process is illustrated in Figure 4.2, where the pyranometer's sensor (red) location is first recorded (a), the map shown is logged using pcolor (MATLAB) to allow for easy identification of the ROI. Following, the ROI is mapped onto the target plane (b), shown by the blue circle, concentric with the instruments base (black). Finally, the perspective corrected irradiance distribution is generated (c).

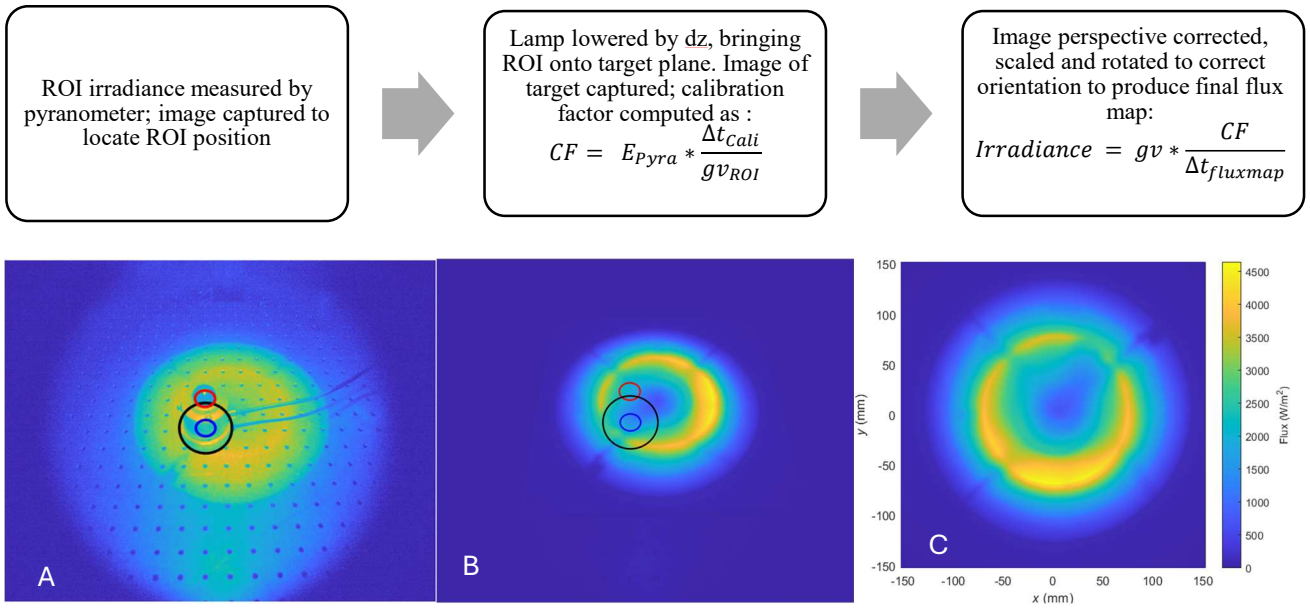

Figure 4.2 *:* Overview of the flux map generation process. (a) CMOS camera captures the pyranometer with the defined region of interest (ROI) offset by + dz. (b) The ROI is superimposed onto the elevated target. (c) The irradiance map is calibrated, perspective corrected and transformed, showing the distribution of irradiance across the target.

To prevent sensor saturation in high-intensity regions, an optical density 3.0 (OD3) filter is applied during all CMOS-based measurements, preserving accuracy across a broad dynamic range. A calibration process is then performed to correlate pyranometer readings with CMOS-derived grayscale values, enabling cross-validation between the two measurement methods and improving the reliability of the final flux maps. The calibration factor (CF) is computed in equation 2 as:

$$CF = E_{Pyra} * \frac{\Delta t_{Cali}}{gv_{ROI}} \quad \text{(Eqn. 2)}$$

where E_{Pyra} represents the pyranometer-measured irradiance, Δt_{Cali} is the exposure time of the calibration image, and gv_{ROI} is the average grayscale value of the ROI. Once calibrated, irradiance maps for new images are generated using equation 3:

$$Irradiance = gv * \frac{CF}{\Delta t_{fluxmap}} \quad \text{(Eqn. 3)}$$

Because the camera is positioned at an angle, the captured images appear trapezoidal, introducing geometric distortion. To correct this, a perspective transformation is applied in MATLAB using the four corners of the target as reference points. This process realigns the images to match the true square dimensions of the target, ensuring accurate spatial mapping of irradiance data. After calibration, grayscale intensity values are converted to irradiance using the calculated calibration factor (CF), creating the flux maps.

The final corrected irradiance map, shown in Figure 3c, provides a comprehensive visualization of the flux distribution, capturing both the intensity of flux gradients of the light source. This correction is essential for precise flux mapping, as it eliminates projection errors and ensures that each pixel corresponds to its actual physical location on the target.

The pyranometer (Kipp & Zonen CM4) measures broadband irradiance using a thermopile sensor that operates over a spectral range of 300–2800 nm, effectively capturing nearly the entire solar and xenon arc lamp spectrum. Its spectrally flat response ensures accurate measurement of total incident power. In contrast, the CMOS camera (FLIR Blackfly BFS-PGE-31S4) is sensitive over a narrower range, primarily 400–1000 nm, encompassing the visible and near-infrared portions of the spectrum. While the camera does not detect the full spectral output of the lamp, this limitation does not impact calibration accuracy. The grayscale-to-flux conversion is performed by averaging the grayscale values within the pyranometer's 1.25-inch ROI and correlating them to the

pyranometer's broadband flux measurement. This establishes a proportional relationship between what the camera sees and the true irradiance. As long as the spectral distribution of the lamp remains constant both in time and in space, this proportionality holds, allowing accurate flux mapping without requiring the camera to sense the full spectral range. Temporal spectral variations are considered negligible, as calibration is performed immediately before image acquisition and the xenon lamp is not expected to cool significantly over time. However, spatial spectral variations across the beam could influence the local grayscale-to-flux calibration. These effects are not currently included in the uncertainty analysis but are the focus of ongoing research.

The combination of a broadband, spectrally flat pyranometer and a spatially detailed camera thus enables robust and high-resolution irradiance characterization.

4.4 Flux Concentration with Fresnel Lens

To investigate the role of optical concentration, a 12-inch Fresnel lens is introduced into the system to enhance the collimated beam's spatial distribution and increase local irradiance. Measurements are conducted at various lamp heights, ranging from 13 to 25 inches in 1-inch increments, to capture a comprehensive understanding of how vertical displacement affects flux concentration. This broad range allows for the identification of key trends in light focusing behavior across a wide range of positions.

Following this initial range, measurements are refined within the 13 to 15-inch range to generate a smoother curve around the inflection point, where significant changes in flux concentration are observed. This finer sampling provides high-resolution data necessary to accurately determine the system's optimal focusing height.

At each increment, grayscale images are analyzed to develop detailed flux profiles, measure the focal length, and identify intensity variations across the illuminated target. This systematic approach allowes for a clear identification of the lamp height that produces the highest localized flux concentration, critical for applications requiring high-precision irradiance control.

The 20 mm focal spot size was estimated by pinpointing regions of maximum power concentration through visual analysis of flux distributions. Beyond this diameter, the flux curve exhibits noticeable flattening, signaling light dispersion and reduced power density.

4.5. Temporal Stability Analysis

The stability of the xenon arc lamp is evaluated by analyzing the normalized root mean square (NRMS) noise, which quantifies fluctuations in light intensity over time. Ensuring temporal stability is crucial for maintaining measurement accuracy and minimizing uncertainty in flux mapping. Variability in irradiance can introduce noise in experimental data, necessitating a systematic approach to characterize and mitigate these fluctuations.

To assess temporal noise, 32 images are captured for each lamp configuration. The evaluation process involved computing NRMS values through a progressive image averaging technique. First, two random images are selected and averaged, followed by another set of two random images, and NRMS is calculated between them. This procedure is systematically repeated for increasing numbers of averaged images (to 16). The NRMS at 32 images is determined through interpolation, allowing for a continuous representation of noise reduction trends.

The NRMS was computed using equation 4:

$$NRMS = \frac{\sqrt{(mean(A-B)^2))}}{\frac{(mean(A)+mean(B)}{2}} \quad \text{(Eqn.4)}$$

where A and B represent independent averaged images from separate randomly selected sets. The numerator quantifies the root mean square deviation between these sets, while the denominator normalizes the deviation by the mean irradiance value. This approach provides a robust metric for evaluating intensity fluctuations across different image averaging conditions.

To analyze the impact of image averaging and exposure time on flux stability, two key approaches are utilized. The first method assessed NRMS as a function of the number of averaged images, determining the effectiveness of image stacking in suppressing noise. The second method examined NRMS as a function of cumulative exposure time, recognizing that exposure durations varied significantly across different configurations, particularly between low-power settings and the highest flux configuration. This approach allows for the assessment of how extended integration affects variability, accounting for the influence of power-dependent flux fluctuation.

5. Results and Discussion

This section presents a thorough analysis of the experimental results obtained from the characterization of the solar simulator. The discussion focuses on three primary aspects: noise analysis and temporal stability, flux mapping results under varying power conditions, and flux concentration using a Fresnel lens. The stability of the system is evaluated through normalized root mean square (NRMS) noise analysis, which provides insights into fluctuations in irradiance over time. Flux mapping results are examined using both direct pyranometer measurements and indirect CMOS camera-based techniques, allowing for a comparative evaluation of the two methods. Finally, the impact of integrating a Fresnel lens for flux concentration is assessed, with a focus on identifying the optimal lamp height and comparing the system's performance to other high-flux solar simulators. These analyses aim to validate the efficiency and effectiveness of the system while identifying areas for potential improvement.

5.1 Noise Analysis and Temporal Stability

The temporal stability of solar simulators is critical for ensuring repeatability and accuracy in experimental setups. Variability in light intensity over time introduces measurement uncertainties that can impact the precision of flux mapping and system characterization. To quantify this stability, a detailed normalized root mean square (NRMS) noise analysis was conducted under different operating conditions, including unfocused low-power mode, unfocused high-power mode, the Fresnel lens best focus configuration and the encircled energy within a 20 mm focal spot of the best focused configuration. The analysis aims to provide insights into the influence of power fluctuations on measurement accuracy and to propose corrective strategies for mitigating instability.

A linear fit was used on the log-log plots to capture the general trend of decreasing NRMS noise with increased averaging. This approach reflects a typical power-law relationship seen in noise reduction. However, the noise does not decrease indefinitely, it eventually levels off. This would appear as a flattening curve on a linear-linear plot, indicating diminishing returns with longer exposure times.

All subsequent flux maps are based on the averaging of 32 images (acquired as two sets of 16 images). The 32-image composite data point, indicated with a star on the plots, is an extrapolation

used to illustrate the expected trend if further averaging was done. The linear fit used in the log-log plots is a conservative estimate of temporal uncertainty. At 32 images, the associated NRMS noise is within an acceptable range (less than 1% at the best configuration and forms the basis for all reported flux measurements.

Figure 5.1 presents the normalized RMS (NRMS) noise values across various lamp configurations and power settings, providing a detailed assessment of the temporal stability of irradiance. The two plots illustrate how NRMS noise varies as a function of (A) the number of averaged images and (B) cumulative exposure time.

The results indicate clear distinctions between low power (blue), high-power (red), and high-power focused with Fresnel lens at 14.25 inches (green). Additionally, the encircled power NRMS data for the 20 mm focal spot of the Fresnel lens best focused configuration (black) showcases the effectiveness of spatial averaging in reducing noise.

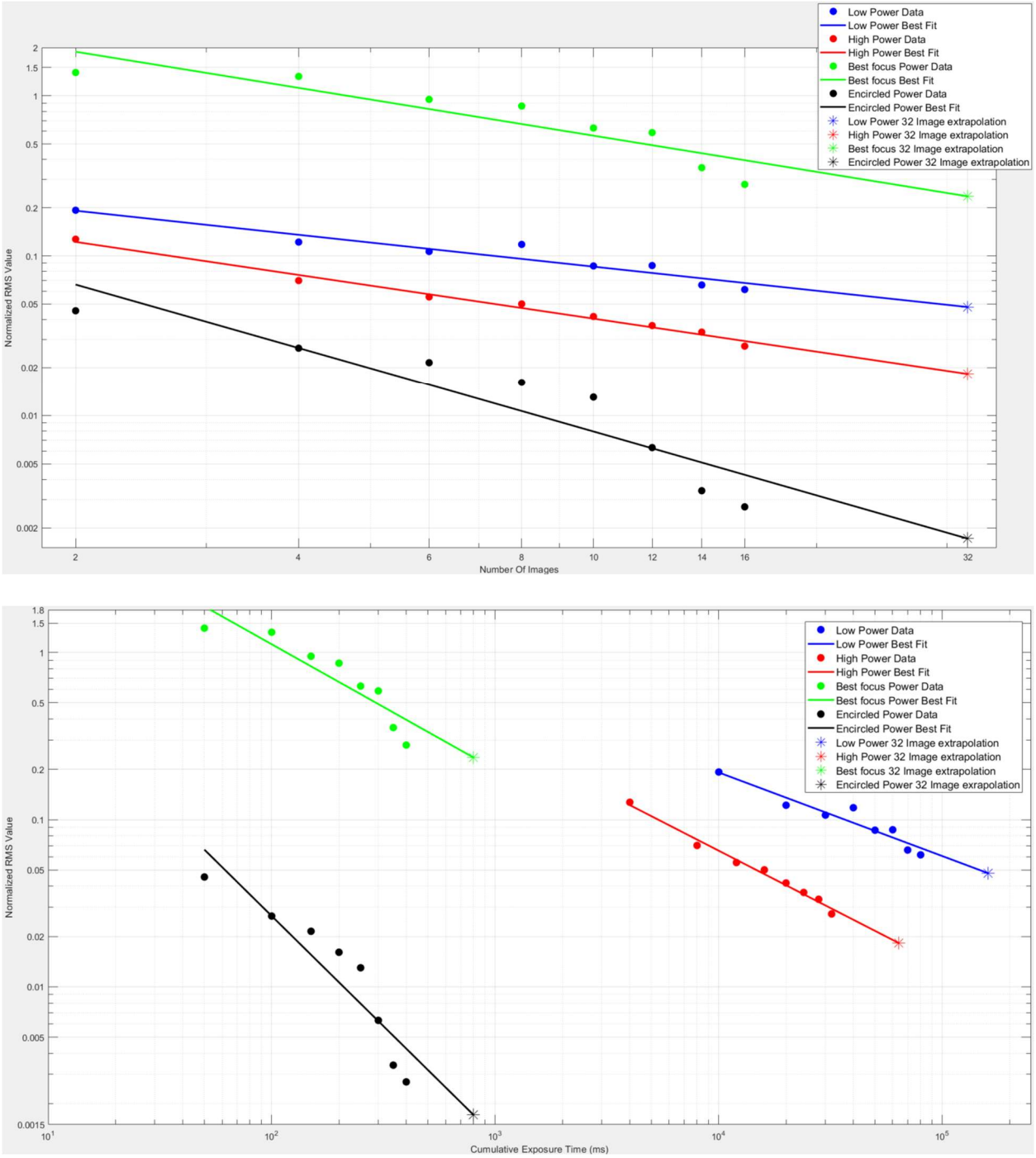

Figure 5.1: Noise analysis of various configurations presented as normalized RMS (NRMS) values. (A) NRMS as a function of the number of averaged images for unfocused low power (blue), unfocused high power (red), best Fresnel focused configuration at 14.25 inches (green), and encircled power of the best focused configuration within a 20 mm spot (black). (B) NRMS as a function of cumulative exposure time for the same configurations.

In the low-power configuration, NRMS noise remains significantly high, with values exceeding 20% even as the number of averaged images increases. This instability arises from the inherent fluctuations in the xenon arc discharge, which become more pronounced at reduced power levels. At lower power, the plasma arc is less stable, leading to erratic motion within the discharge chamber. Additionally, the lower plasma temperature makes the system more susceptible to electrode wear and environmental disturbances such as minor air currents or temperature fluctuations. Small variations in the power supply further contribute to inconsistencies in irradiance output. The NRMS noise gradually decreases as more images are averaged, but even after 32 images, it remains above 5%, indicating that low-power operation does not provide sufficient stability for precision applications requiring highly consistent irradiance.

In contrast, the high-power configuration exhibits significantly improved temporal stability. NRMS noise starts at a lower value and decreases steadily as additional images are averaged, ultimately dropping below 2% after 32 images. This improvement is primarily attributed to a more stable arc discharge, maintained by the higher thermal energy at full power. The increased energy density stabilizes plasma formation, ensuring more consistent light output and minimizing intensity fluctuations. Additionally, electrode degradation has a reduced impact at higher power, as the arc remains more consistent over time. The higher intensity-to-noise ratio at full power also helps suppress relative fluctuations in irradiance. In Figure 5.1A, the red data points follow a well-defined trend, indicating a predictable and steady reduction in noise with increasing image averaging. Similarly, Figure 5.1B shows a clear decline in NRMS noise as cumulative exposure time increases, emphasizing the role of longer exposure durations in integrating and stabilizing the irradiance output. This trend confirms that operating at high power provides a significantly more reliable irradiance source, suitable for experiments requiring precise and repeatable flux measurements. Furthermore, the reduced influence of external perturbations in the high-power configuration makes it particularly well-suited for applications demanding stable long-term illumination, such as thermal material testing and solar energy device calibration.

The introduction of a Fresnel lens at a height of 14.25 inches significantly alters noise characteristics. In this configuration, NRMS noise is substantially higher, with initial values exceeding 200%. Several factors contribute to this increased instability, including optical aberrations and minor misalignments, which create localized variations in flux intensity. The

Fresnel lens also amplifies inherent lamp fluctuations by focusing the irradiance onto a smaller area, making the system more sensitive to slight variations in positioning. Despite the increased noise, the green dataset in Figure 5.1B follows the same downward trend as the high-power configuration without the lens, demonstrating that extended exposure durations reduce fluctuations. However, the extreme concentration of flux introduces additional challenges, as small variations in positioning or alignment result in amplified instability.

The encircled power dataset within the 20 mm spot, taken from the Fresnel lens best focus configuration at 14.25 inches, provides strong evidence for the effectiveness of spatial averaging in reducing noise. Unlike individual pixel-based measurements, which capture localized fluctuations, this method integrates irradiance over a broader area, significantly improving stability. The power fluctuation within this region is much lower, reinforcing the reliability of the spatial averaging approach. After 32 image averages, NRMS noise falls below 0.2%, making this configuration the most stable among those tested. The relationship between cumulative exposure time and noise reduction, as shown in Figure 5.1B, further supports the importance of extended integration periods for achieving consistent irradiance. These findings highlight the advantages of spatial averaging for applications requiring temporal stability, as it effectively mitigates localized fluctuations and enhances measurement reliability. The ability to integrate flux across a region instead of relying on single-pixel data allows for a more robust and realistic representation of irradiance, ensuring that minor variations in the beam profile do not introduce significant experimental errors.

The results emphasize the necessity of longer exposure durations to improve stability. Short exposure times capture transient fluctuations, leading to artificially high noise levels. In contrast, longer integration periods allow the system to smooth out variations, producing more consistent measurements. Overall, the findings highlight the effectiveness of high-power operation and spatial averaging in stabilizing irradiance fluctuations. While challenges remain in mitigating noise at high flux concentrations, extended exposure times and optimized configurations significantly improve measurement consistency. These insights reinforce the importance of refining experimental setups to balance intensity, stability, and repeatability for advanced solar simulation applications.

5.2 Flux Mapping Results

Flux mapping was conducted using both direct pyranometer-based measurements and indirect CMOS camera-based techniques to gain a comprehensive understanding of the spatial distribution of irradiance and the total radiant power output at different power levels. This analysis is crucial for validating the effectiveness of indirect flux mapping methods in solar simulation applications and assessing their accuracy relative to direct measurement techniques. Due to the limitations of the pyranometer at irradiance levels above 4 suns, CMOS-based flux mapping was the primary method used for high-power and concentrated high flux configurations.

5.2.1 Flux Distribution at Low Power

In the low-power configuration, the pyranometer recorded an average flux of 908 W/m², corresponding to a total power output of 84 W over the 12 × 12-inch Lambertian target area. The CMOS camera-based flux mapping method, however, measured a slightly higher average flux of 1092 W/m² with a computed power of 98 W. This 14% discrepancy between the two methods likely results from differences in integration time, spatial averaging, and variations in sensor response. Additionally, positional misalignments and differences in spectral sensitivity between the pyranometer and the CMOS sensor may have contributed to the observed differences.

To improve measurement accuracy, three separate pyranometer datasets were averaged, yielding a total of 144 data points, which were then mapped onto a 12 × 12-inch grid. The resulting flux map, shown in Figure 5.2, depicts a central high-intensity region that gradually diminishes towards the edges. This visualization provides insight into the flux distribution across the target surface.

For the indirect CMOS flux mapping approach, Figure 5.3(A) presents the contour-style flux map of the low-power configuration obtained. This map offers a broader perspective on the spatial distribution of irradiance. This representation smooths out localized variations and emphasizes the overall irradiance gradient across the target surface. Comparing this visualization with the flux map generated form the pyranometer points allows for an evaluation of irradiance uniformity, confirming that while the pyranometer effectively captures overall trends, the CMOS camera provides a more detailed and continuous representation of spatial flux variations.

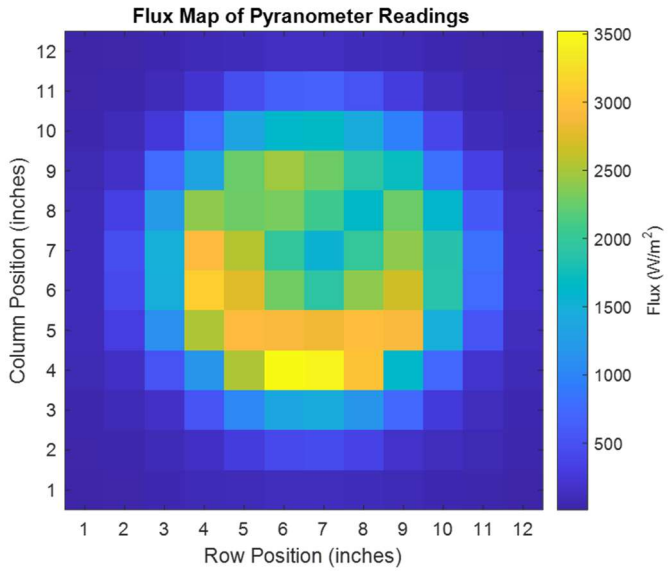

Figure 5.2: Flux map of pyranometer readings using the averaged dataset of three measurements, mapped onto the 12 × 12-inch grid.

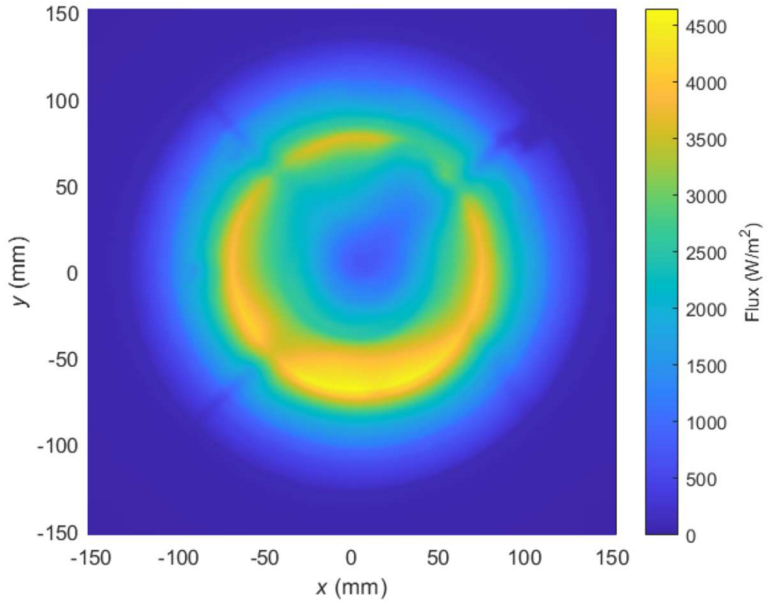

Figure 5.3 (A): Contour-style flux map of the square target at low power, illustrating the irradiance distribution of the xenon lamps unfocused light.

For a more resolution direct comparison, the CMOS generated image was grided into a 12x12 inch grid to match the resolution of the pyranometer. Circular ROIs were then drawn in the center of the square grid points to mimic the location of the pyranometer. The average flux value was then calculated for each of the 144 ROIs. Figure 5.3(B) is then plotted to directly compare the CMOS method to the pyranometer method at the same resolution.

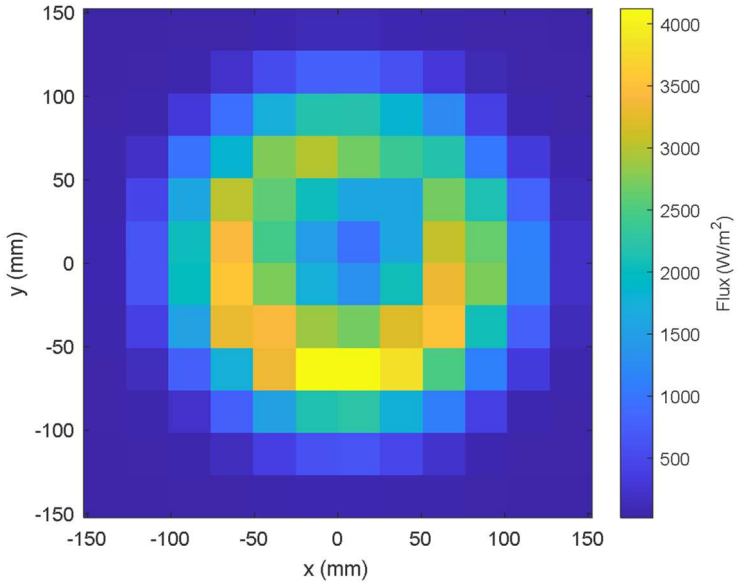

Figure 5.3 (B): Flux map of the square target at low power, constructed by averaging the CMOS camera-derived irradiance within 1.25-inch diameter circular regions arranged over a 300x300 mm (12 × 12-inch) grid.

Building on this analysis, Figure 5.4 presents a 3D flux map of the low-power configuration generated by the CMOS camera, with the pyranometer sensor grid superimposed. The color scale represents flux in W/m², while the red circles indicate the 1.25-inch diameter pyranometer sensing areas, systematically arranged over the 12 × 12-inch (300 x 300 mm) grid. This visualization highlights the contrast in spatial resolution between the two techniques, illustrating how the CMOS camera captures finer irradiance variations, whereas the pyranometer provides discrete point-based measurements at fixed positions.

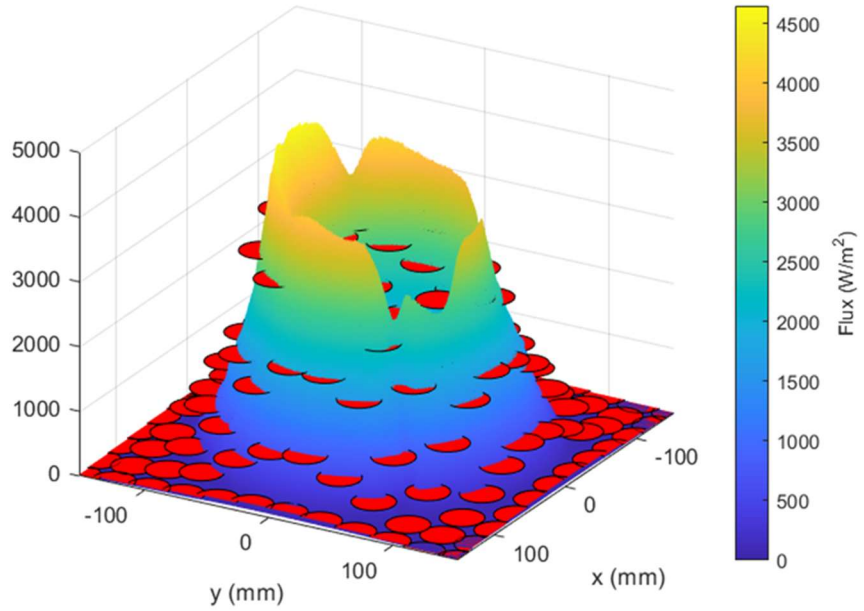

Figure 5.4: flux map of the low-power flux map with superimposed pyranometer sensor grid. The color scale represents flux in W/m², while the red circles indicate the 1.25-inch diameter pyranometer sensing areas, arranged in a 12x12 inch grid across the target surface.

A key factor contributing to the discrepancy between the two flux maps is the difference in integration time and spatial resolution between the sensors. The pyranometer has a significantly longer integration time, meaning its readings represent a time-averaged flux over its sensing duration, smoothing out rapid fluctuations in irradiance. Additionally, each measurement captures an average flux over the 1.25-inch diameter sensing area, inherently reducing localized variations and leading to a lower spatial resolution. In contrast, the CMOS camera records flux with much shorter exposure times, preserving finer details and capturing higher peak values, which likely explains the overall higher irradiance distribution observed in the CMOS flux map.

Another contributing factor is gaps in the pyranometer dataset, particularly along the diagonal of the measurement grid, where no data points were recorded. These missing measurements require interpolation, introducing additional uncertainty when reconstructing the flux map. Conversely, the CMOS camera provides a continuous spatial distribution, capturing irradiance variations across the entire target area without the need for interpolation. Despite these differences, both methods produced comparable total power estimations, reinforcing the reliability of indirect flux mapping in solar simulation. However, the higher spatial resolution of the CMOS camera makes it more

effective for identifying localized flux variations, whereas the pyranometer remains valuable for point-based flux validation and calibration.

Overlaying pyranometer readings onto the flux map shows a high degree of agreement between the two methods, reinforcing the accuracy and consistency of both measurement approaches. However, slight deviations were observed due to differences in exposure settings and the inherent averaging effects of the pyranometer, which may have influenced the final flux estimations.

Further examination of both the pyranometer and CMOS flux maps revealed an annular irradiance distribution, where the highest flux intensities form a ring around the center rather than peaking at a single central point, with a gradual intensity decrease toward the periphery of the target area. This distribution can be attributed to the construction of the lamp itself. The xenon lamp is centrally positioned within a cylindrical housing that contains internal reflectors. Below the lamp, several fixture components obstruct direct light from escaping, casting a shadow that reduces irradiance in the central region. As a result, the highest flux intensities form a ring around the center rather than producing a uniform disk of light. This structural feature explains the observed annular irradiance pattern.

The flux map analysis also confirmed that light spillage beyond the target region was negligible in the low-power configuration. Stray flux levels remained below 1 W/m^2, primarily due to negligible background noise from ambient lighting, which persists even when the lamp is off. This reinforces that the optical system effectively constrained the light to the intended area without significant external interference.

These findings highlight the complementary nature of the two measurement techniques. The pyranometer, with its longer integration time and averaging over a 1.25-inch sensing area, provides stable and reliable total power estimates but lacks the spatial resolution needed to detect localized flux variations. Conversely, the CMOS-based mapping method captures fine-scale irradiance details and non-uniformities, but its shorter exposure time may introduce fluctuations not observed in the pyranometer data.

By using both methods together, their respective strengths compensate for individual limitations. The pyranometer ensures calibrated and consistent power validation, while the CMOS camera provides high-resolution spatial flux mapping. This combined approach improves the accuracy and

reliability of solar simulator characterization, offering a more complete understanding of irradiance distribution for experimental applications.

5.2.2 Flux Distribution at High Power

At high power, the pyranometer was unable to capture measurements due to its upper detection limit of 4 suns, necessitating the exclusive use of CMOS flux mapping. Under these conditions, the flux distribution demonstrated significant improvements, with an average flux of 2819 W/m² and a total power output of 254 W over the 12 × 12-inch target area.

Figure 5.5 presents the flux distribution at high power, illustrating the spatial variation in irradiance across the target surface. The highest flux intensities form a distinct ring surrounding the central region, like the low-power case but with significantly greater intensity. This pattern is attributed to the lamp's cylindrical construction and the presence of internal fixture components that partially obstruct direct light emission. The two diagonal line shadows, more pronounced in this map, correspond to the crossbars supporting the xenon bulb fixture, creating localized reductions in flux intensity. Despite these minor irregularities, the overall flux distribution remains well-contained within the target area.

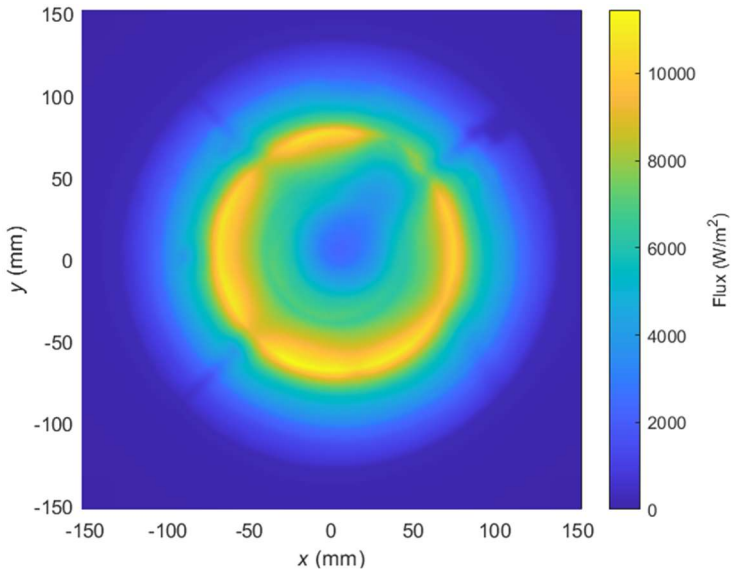

Figure 5.5: Flux map of the square target at high power, illustrating the irradiance distribution of the xenon lamps unfocused light.

5.3 Lamp Efficiency:

The efficiency of the xenon arc lamp was assessed under both low- and high-power configurations to evaluate its energy conversion performance. At low power, the lamp consumed 628 W, yielding an efficiency of 13.4% based on pyranometer measurements and 15.6% from flux mapping data. These differences stem from the inherent variations in measurement techniques—while the pyranometer provides direct power readings at discrete points, flux mapping integrates multiple spatially resolved measurements to generate an overall power distribution. The slight variation between these methods underscores the importance of employing multiple validation techniques to ensure accurate efficiency assessments.

In the high-power configuration, the input power increased to 1137 W, with a corresponding output power of 254 W, resulting in an efficiency of 22.4%. This improvement is primarily due to the reduced impact of fixed power losses. Components such as the power supply and cooling fans maintain relatively constant energy consumption, meaning their share of total power consumption decreases as lamp power increases. This trend demonstrates that operating at higher power levels allows for more efficient conversion of electrical energy into radiant output.

Table 5.1 presents the power consumption characteristics of the system under various operational states. These measurements provide insights into how power is distributed across different components:

Operational State	Power (W)	Voltage (V)	Current (A)	Power Factor (PF)
No Load (System Off)	0	120.8–121.0	0	1.00
Power Supply Only	56.6–58	120.7	0.63	0.74
Main System On (No Lamp)	60.5–60.9	120.7	0.65l	0.76
Lamp On (Initial Ignition)	113	121.0–123.0	1.44	0.63
Low Power Mode	628–635	118.6–118.8	8.52–8.57	0.62
High Power Mode	1137–1142	116.6	13.94–14.0	0.70

Table 5.1: Consumption characteristics of the system under various operational states. These measurements provide insights into how power is distributed across different components

The power factor (PF) at high power is 0.70, compared to 0.62 at low power, indicating improved electrical efficiency as power increases. A higher power factor suggests a more effective conversion of electrical energy into useful work, reducing losses associated with reactive power. Additionally, the power supply and control electronics consistently draw approximately 60 W, independent of lamp operation. As this baseline consumption remains constant, it constitutes a smaller proportion of total power use at high power, effectively increasing system efficiency. The consistent auxiliary power consumption indicates that efficiency gains at higher power levels result as well as more effective energy conversion.

Efficiency improves significantly at high power, where the xenon lamp operates most effectively. The power factor (PF) increases from 0.62 to 0.70, reflecting better electrical efficiency and reduced energy losses. The power supply and control electronics draw a constant 60 W, but as lamp power increases, this fixed consumption becomes a smaller fraction of total energy use. As a result, more input power is converted into useful radiant output, while fixed losses have a diminishing impact. High-power operation not only enhances flux output but also optimizes energy utilization, making it the most efficient mode.

Figure 5.6 provides a visual breakdown of power distribution at both low and high-power levels, illustrating the contributions of electrical input, power loss, auxiliary power consumption, and

radiant output. The graph clearly demonstrates that at high power, a larger proportion of input energy is effectively converted into radiant output, while auxiliary losses remain largely unchanged. This observation reinforces the advantages of operating the lamp at maximum capacity to optimize energy conversion and minimize the fraction of power lost to non-productive components.

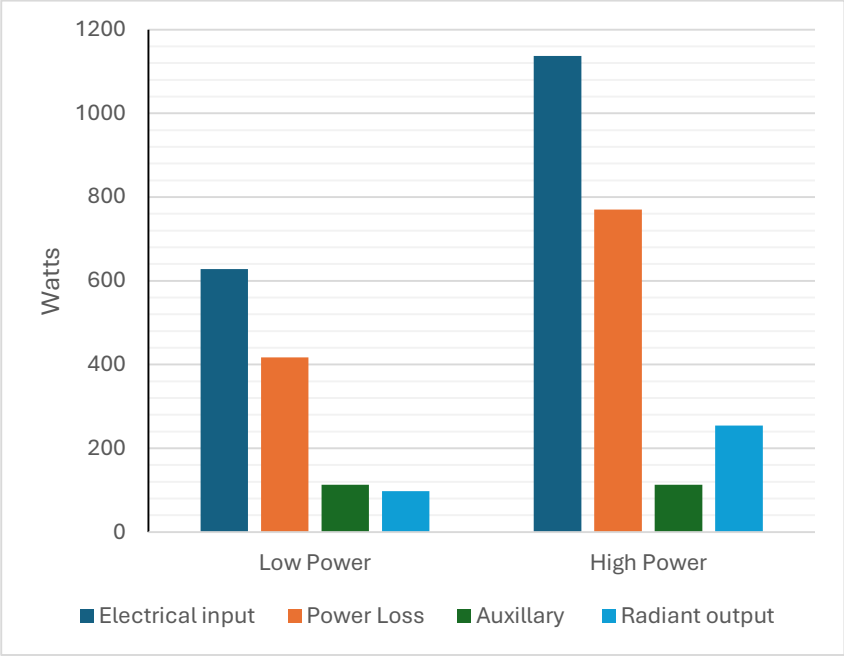

Figure 5.6: Power distribution breakdown at low and high power, illustrating the contributions of electrical input, power loss, auxiliary power consumption, and radiant output.

5.4 Flux Concentration Using a Fresnel Lens

This section presents experimental findings on using a Fresnel lens to condense and concentrate irradiance from a xenon arc lamp. The main objective was to concentrate flux by focusing all the light onto a smaller target area.

The lamp was initially positioned at a height of 25 inches and systematically lowered in 1-inch increments down to 13 inches, with the Fresnel lens fixed relative to the lamp. This adjustment led to a progressive concentration of the light, as the flux became increasingly focused toward the target area. Figure 5.7 illustrates the corresponding flux maps at selected heights (25, 23, 21, 19, 17, and 15 inches), demonstrating the gradual enhancement of flux intensity and spatial focus as the system neared the optimal focal point.

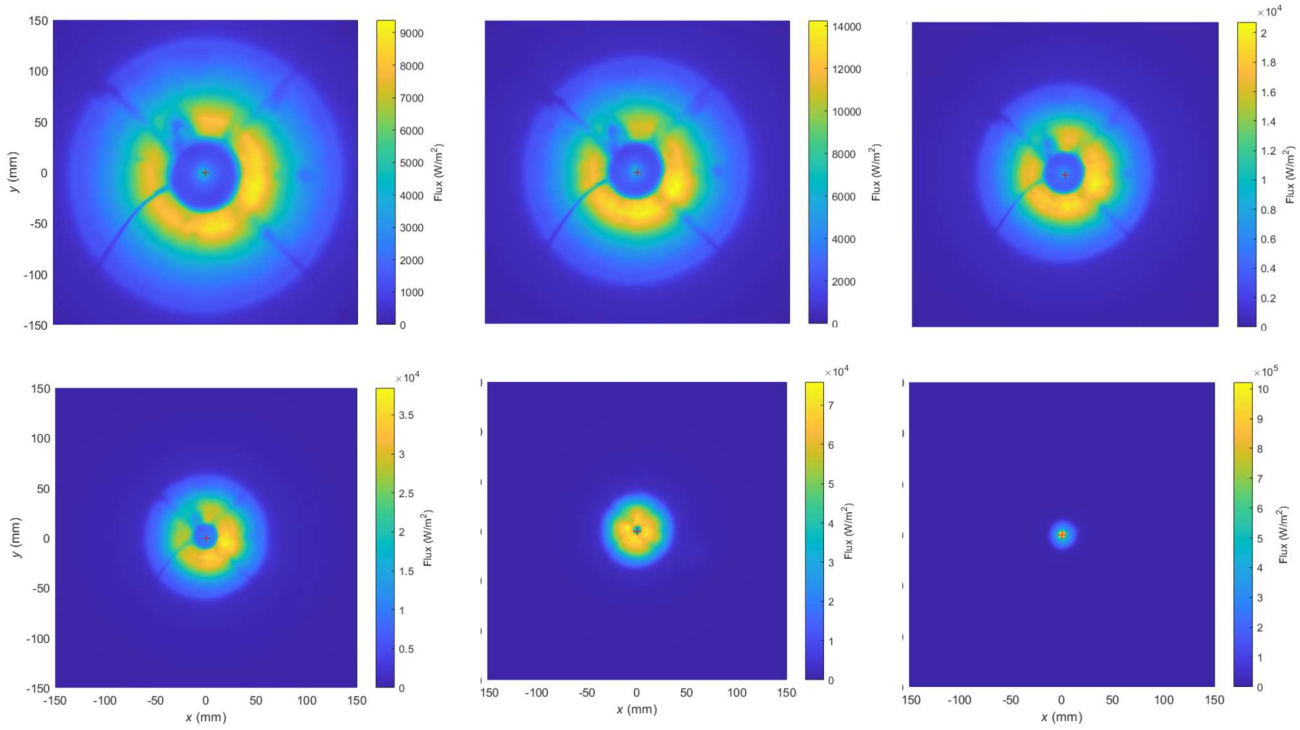

Figure 5.7: Flux maps at varying lamp heights as the lamp is systematically lowered in 1-inch increments. Each plot shows the irradiance distribution across the target surface at heights of 25 (top left), 23, 21, 19, 17, and 15 inches (bottom right).

The relationship between lamp height and flux concentration became evident as the lamp was lowered, intensifying the irradiance into a more concentrated beam. The focusing effect improved progressively, peaking at 14.25 inches. Once the lamp was lowered beyond this point to 13 inches, additional measurements were performed by raising the lamp in 0.125-inch increments from 13 to 15 inches. This refined testing was conducted to gather more data near the inflection point of the flux curve, ensuring smoother graphing and providing a clearer understanding of the system's behavior around the optimal focal height. The results revealed that surpassing this point diminished concentration, leading to a broader and less focused beam.

Figure 5.8 presents the refined flux distribution at heights of 13.75 inches, 14.0 inches, and 14.25 inches, clearly depicting the narrowing beam and optimal flux concentration achieved at the ideal focal point.

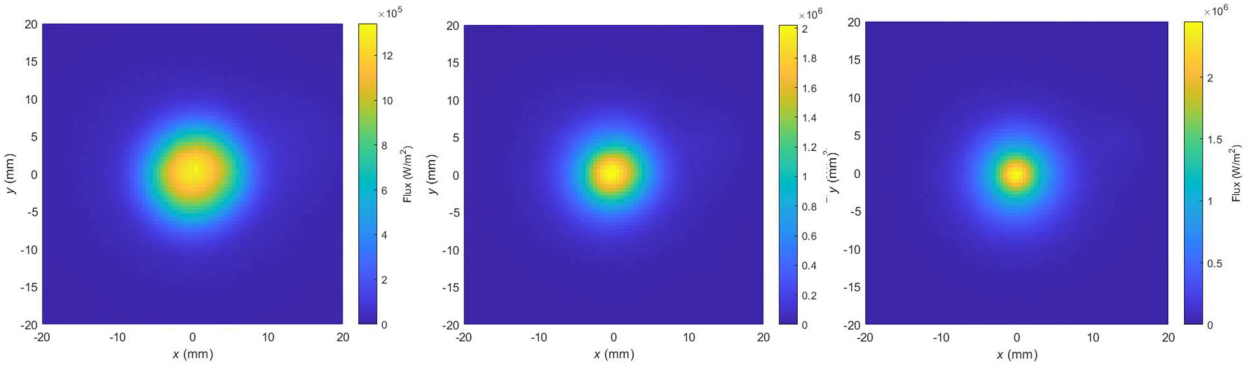

Figure 5.8: Flux maps at varying lamp heights. Each plot represents the irradiance distribution captured across the target surface. The maps correspond to height configurations: 13.75(left), 14.0, 14.25 (right) (inches from table).

Figure 5.9 presents the relationship between lens height and both the average flux and total power output, calculated from flux measurements within a 20 mm diameter spot. Both metrics peaked at a height of 14.25 inches, highlighting the critical importance of precise lens positioning for achieving maximum irradiance concentration. The graph reveals a clear asymmetry in the system's sensitivity to height variations. As the lamp approaches 14.25 inches, both power and flux increase sharply, indicating a rapid intensification of energy focus. However, after surpassing this optimal height, there is a pronounced and rapid decline in both metrics. This sharp drop is attributed to beam divergence, where the focused light begins to spread over a larger area.

Further analysis focused on how spot size influenced both average irradiance and total power output. A peak flux of 2348 kW/m² was achieved using the Fresnel lens, with the system successfully concentrating 59.8% of the total lamp power onto a 20 mm spot size. Notably, this peak flux value was derived from a single-pixel reading, demonstrating the system’s ability to produce highly localized, intense concentrations of light. As shown in Figure 5.10, increasing the spot diameter led to a noticeable reduction in average irradiance due to the distribution of concentrated energy over a larger area.

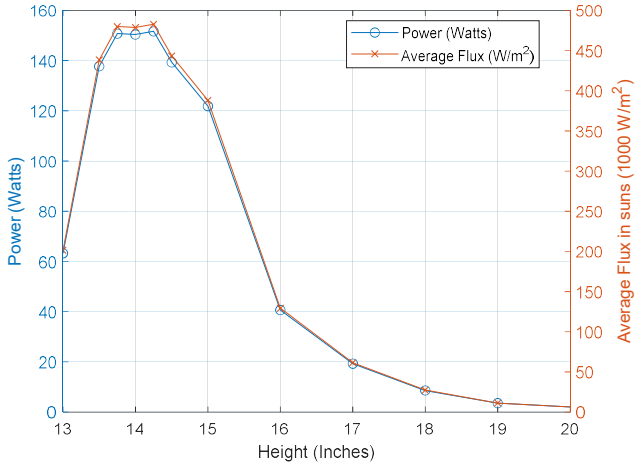

Figure 5.9: Average flux(red) and total calculated power(blue) of a 20 mm diameter spot as a height of the lamp is varied.

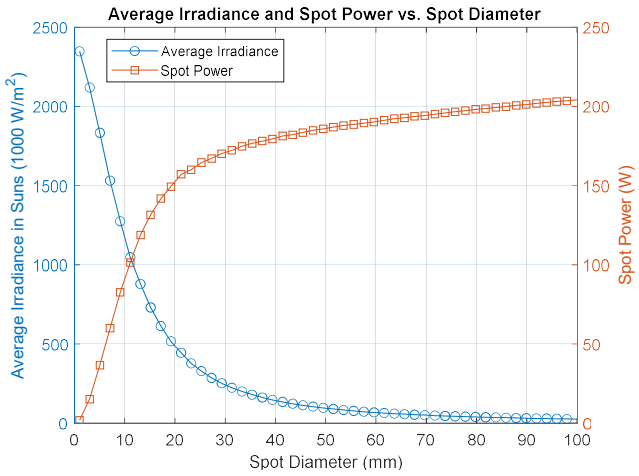

Figure 5.10: Average irradiance(blue) and calculated spot power(red) as a function of spot diameter.

These results highlight the Fresnel lens's ability to significantly enhance flux density over a small target area, concentrating approximately 59.8% of the total lamp power into a 20 mm spot, producing an average flux of 483 kW/m² and a total concentrated power output of 152 W. This configuration was also used to determine the optimal spot size for the noise analysis section, as the best-performing setup was employed for capturing the 32 images required for that analysis. Even slight deviations from this height led to noticeable reductions in flux density and power output.

Total spot power initially increased with larger spot sizes but plateaued around a diameter of 100 mm. Beyond this point, the lens became less effective at maintaining any light concentration. The 20 mm spot size selected provides an effective balance of high irradiance and maximum power, while being a practical spot size for many solar thermal applications.

5.5 Uncertainty Analysis

To ensure the reliability of irradiance measurements obtained via both direct (pyranometer) and indirect (CMOS camera) methods, an uncertainty analysis was conducted. Each identified source of uncertainty was classified and quantified based on sensor specifications, calibration data, and image-based evaluation.

5.5.1 Direct Measurement (Pyranometer-Based)

Calibration Uncertainty:

The pyranometer used in the direct flux mapping method has a manufacturer-specified calibration uncertainty of $< \pm 1\%$ under stable irradiance.

Positioning Uncertainty:

Manual placement accuracy across the 12 × 12-inch grid was maintained within ±1 mm, minimizing spatial registration error during scanning.

5.5.2 Indirect Measurement (CMOS-Based)

Camera Non-Linearity:

The CMOS sensor (FLIR Blackfly S) operates linearly across the relevant signal range. Residual non-linearity is estimated at ±1%, consistent with vendor specifications.

Sensor Nonuniformity (Flat Field Analysis):

A flat field image was captured using a calibrated integrating sphere to characterize spatial response of the camera sensor. A region of interest was manually drawn using a circular ROI covering the central uniform zone. The extracted pixel values had a mean of 0.756 and a standard deviation of 0.027, yielding a coefficient of variation of 3.6%, which is used as the uncertainty from pixel-level nonuniformity.

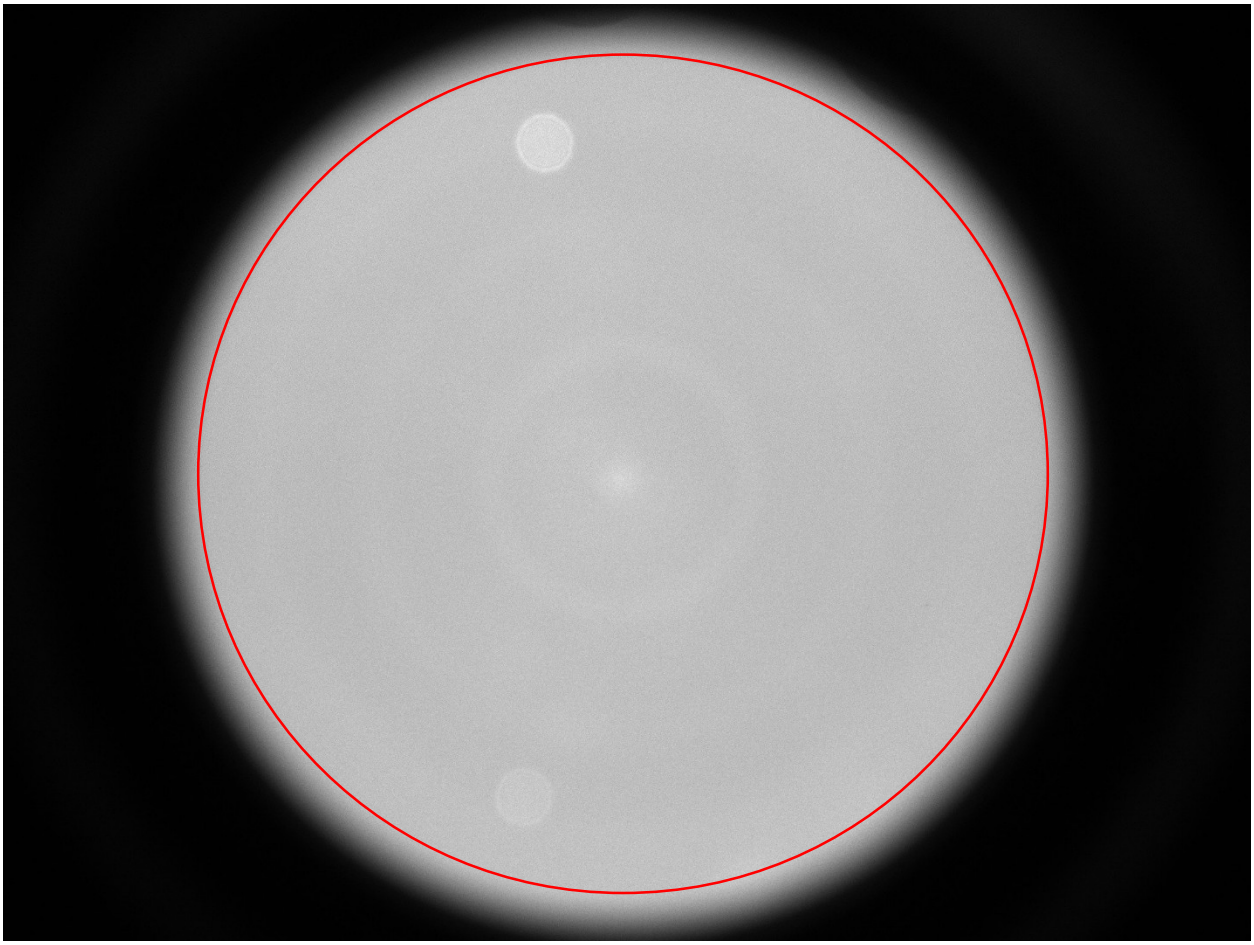

Figure 5.11: Normalized flat field image (0–1 scale), captured using an integrating sphere. The red circle indicates the region analyzed for sensor uniformity. Pixel variation within this region supports a spatial nonuniformity uncertainty estimate of ±3.6%.

This source of uncertainty can be further minimized through flat field correction, where each relative flux map is divided by the normalized flat field image to account for spatial variations in the sensor's response.

5.5.3 Combined Uncertainty

A root-sum-square (RSS) method was used to combine the uncertainties in the CMOS-based measurement system:

Source	Uncertainty
Pyranometer calibration	±1%
Camera non-linearity	±1%
Flat field nonuniformity	±3.6%
Lamp temporal fluctuation	±1%

$$Total = \sqrt{(1\%)^2 + (1\%)^2 + (3.6\%)^2 + (1\%)^2} = 4\% \qquad \text{eqn.5}$$

This uncertainty represents one standard deviation. For a confidence level of 95%, a coverage factor of 2 is applied, yielding an uncertainty, U of 8%. This value represents the overall uncertainty in indirect flux mapping and is used when reporting power, irradiance, and efficiency values derived from camera-based measurements. It should be noted that this is calculated using the best encircled energy of the best configuration.

5.6 Simulator Classification

To formally assess performance, the solar simulator was evaluated according to the standard criteria defined by ASTM E927: spectral match, spatial uniformity, and temporal stability.

Spectral mismatch:

Xenon arc lamps are commonly employed in solar simulators due to their broad spectral output and high radiative intensity. However, their emission spectrum differs from the ASTM AM1.5 Global solar reference, particularly in the near-infrared (NIR) region. As reported by Gallo et al. [32], approximately 49% of the xenon arc lamp's radiative power is emitted above 800 nm, compared to 37% for natural sunlight. Within the visible range (300–700 nm), xenon emits 67% of its power, while the sun emits 63%.

To evaluate the spectral match under ASTM E927, the xenon lamp spectrum was integrated across six defined wavelength bands from 400 nm to 1100 nm and compared to the AM1.5 reference spectrum. The spectral match for each band is quantified using the ratio of the simulator's relative spectral intensity in each band against the corresponding AM1.5 value. ASTM then assigns a class based on this deviation from unity.

Band (nm)	Xenon Arc (%)	AM1.5 (%)	Spectral match ratio	ASTM Class
400–500	15.36	18.4	0.835	A
500–600	16.23	19.9	0.816	A
600–700	13.92	18.4	0.757	A
700–800	10.71	14.9	0.719	B
800–900	17.94	12.5	1.435	C
900–1100	25.79	15.9	1.622	C

Table 5.2: Spectral match classification of the xenon arc lamp based on ASTM E927. The percentage of total spectral intensity in each band (400–1100 nm) is compared to the Global AM1.5 reference.

The results are summarized in Table 5.2. The simulator meets Class A requirements across the visible spectrum (400–700 nm), but falls to Class B in the 700–800 nm band and Class C beyond 800 nm. Therefore, an overall spectral match classification of Class C is assigned, as required by ASTM E927's criterion that the final rating corresponds to the lowest-performing band.

In addition to this spectral deviation, xenon arc lamps also exhibit spatial variation in spectral content across the arc gap. Nakar et al. [33] demonstrated that the hottest region near the cathode tip emits primarily in the visible and near-infrared, whereas cooler regions, particularly the electrodes emit more strongly in the mid-infrared. As a result, the effective spectrum reaching the target is influenced by the optical system's geometry and which regions of the arc are preferentially collected or imaged. This spatial dependence is particularly relevant when using detectors with wavelength-dependent sensitivity. In this study, spectral variation across the arc was not explicitly corrected and is instead encompassed within the overall spectral mismatch uncertainty.

Temporal Instability:

To evaluate the temporal stability of the solar simulator under different configurations, 32 consecutive camera images were acquired for each of the low-power, high-power, and best-focus settings. For each pixel, the standard deviation across the image stack was computed and normalized by the mean pixel intensity to yield the relative temporal uncertainty, u= $\frac{\sigma}{\mu}$. This was then scaled to a 95% confidence interval by applying a coverage factor k = 2 yielding the final uncertainty, U= 2u, expressed as a percentage Figure. 5.12 shows the uncertainty maps across 32 images for low, high, and best focused configurations.

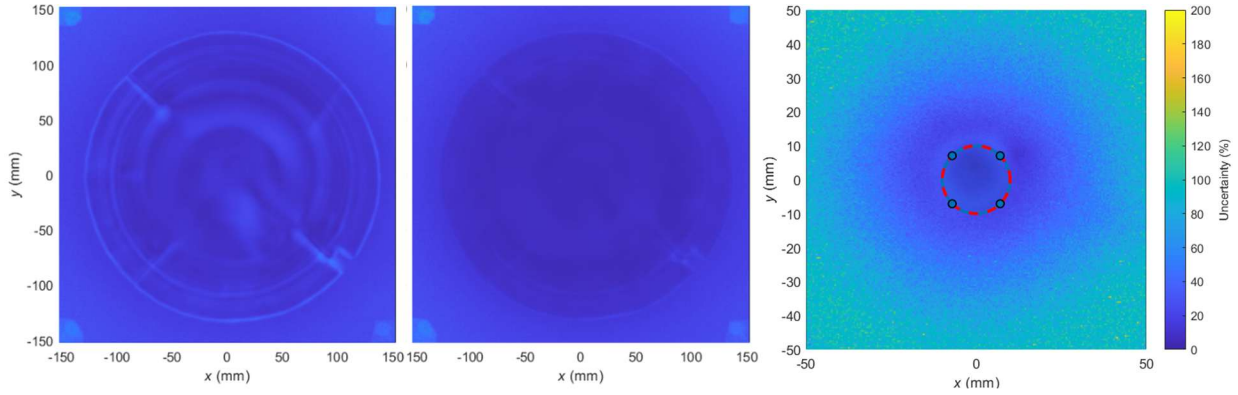

Figure 5.12: Temporal uncertainty maps for low-power (top left), high-power (top right), and best-focus (bottom) configurations.

Temporal stability was assessed in accordance with ASTM E927 by evaluating the variation in irradiance over 32 consecutive camera images for each operating configuration. A circular region of interest (ROI) was defined to represent a typical device under test (DUT). For the low- and high-power configurations, a 200 mm diameter ROI was used, while a 20 mm diameter ROI was applied for the best-focus case to reflect the localized nature of the concentrated beam. Table 5.3 shows the resulting uncertainty for each of the cases.

Configuration	ROI Diameter	Temporal Uncertainty	ASTM Class
Low Power	200 mm	4.90%	B
High Power	200 mm	3.97%	B
Best Focus	20 mm	4.50%	B

Table 5.3: ASTM E927 temporal stability classification of the solar simulator for three operating configurations.

The standard deviation of average irradiance within the ROI was computed for each configuration and normalized by the mean to obtain the relative temporal uncertainty. A coverage factor of k=2 was applied to reflect a 95% confidence interval. The resulting uncertainties were 4.90% (low power), 3.97% (high power), and 4.50% (best-focus). According to ASTM E927, all three cases fall within the requirements for Class B temporal stability (≤5%), indicating moderate fluctuations in lamp output.

Spatial uniformity:

Up to this point, no effort was made to achieve a spatially uniform flux distribution, as the simulator was primarily designed and optimized for concentrated flux applications. As discussed in Section 5.6, the spatial profile under typical focused operation is highly non-uniform, with a steep irradiance gradient near the focal spot. However, in Chapter 6, a ground glass diffuser was introduced into the optical path to adapt the system for low-flux, uniform irradiation scenarios such as radiative cooling experiments. The diffuser was positioned to homogenize the beam before it reached the target. While this reduced the peak flux, it produced a more even irradiance distribution across the measurement area. In a 5 × 5 measurement grid, the recorded signal ranged from 10.3 mV to 10.6 mV, corresponding to flux values between 1.117 kW/m² and 1.150 kW/m². Using the ASTM E927 definition, the spatial non-uniformity is calculated using equation 5.1:

$$Non - unifomity = 100 * \frac{Emax-Emin}{Emax-Emi} = 1.46\% \qquad \text{(eqn. 5.1)}$$

This result satisfies the Class A requirement (≤ 2%) for spatial non-uniformity under ASTM E927. These findings highlight the simulator's adaptability for uniform, low-flux testing applications by simply incorporating a passive diffuser element. Without diffusion, the non-uniformity is calculated at over 73% in the low power case and 66% in the high power case.

5.7 Comparison with Other High-Flux Solar Simulators

This section compares the performance of the commercial xenon searchlight-based solar simulator with various other high-flux solar simulators (HFSS) documented in recent literature. The comparison highlights the system's performance in terms of peak flux, average flux, efficiency, and flux mapping methodologies.

Ekman et al. (2015) constructed a 42 kW solar simulator employing seven 6 kWe metal halide lamps, achieving a peak flux of approximately 927 kW/m² at the secondary focal plane [1].

Sarwar et al. (2014) investigated a 7 kW xenon lamp-based solar simulator combined with an ellipsoidal reflector. This configuration achieved a peak flux of 3583 kW/m² at 153 A and demonstrated an efficiency of approximately 47%, with a reported temporal instability of less than 3% [4]. The tunability range of the flux from 2074 to 3583 kW/m² provided flexibility similar to the cinema searchlight configuration, facilitating adaptability for diverse research needs.

Krueger et al. (2011) presented a 45 kW simulator incorporating seven xenon lamps, each integrated with ellipsoidal reflectors to enhance flux concentration. This configuration delivered approximately 7.5 kW of power onto a 6 cm diameter target area, achieving a peak flux of around 3.7 MW/m² [11]. The multi-lamp arrangement described aligns well with potential future expansions involving multiple xenon lamps.

Zhu et al. (2020) designed and characterized a powerful 130 kW solar simulator featuring 13 xenon lamps. This setup produced a remarkable peak flux exceeding 11 MW/m² and maintained an average flux of approximately 1 MW/m² across a large 200 mm diameter target [10]. Such sophisticated arrangements illustrate the high potential achievable through careful alignment and utilization of multiple high-power xenon lamps.

Wang et al. (2017) introduced a Fresnel lens-based solar simulator consisting of 12 xenon lamps, achieving a peak flux of 7.22 MW/m² and an overall efficiency of about 23.4% [6]. This innovative approach provided excellent flux distribution and strong efficiency, making it a highly attractive option for potential system expansion.

Compared to these sophisticated systems, the single-lamp, 1 kW xenon cinema searchlight simulator demonstrated highly competitive performance. It achieved a peak flux of 2348 kW/m² through an integrated Fresnel lens setup, effectively concentrating approximately 60% of the

lamp's total power onto a 20 mm diameter spot. Direct flux measurements conducted with a pyranometer indicated an average flux of 2819 W/m² at high power operation, achieving an efficiency around 22.4%. Indirect flux measurements obtained using a CMOS camera supported these results, confirming reliability and consistency.

Additionally, the integrated methodology combining direct and indirect flux mapping techniques provides significant benefits over traditional methods. For example, Xiao et al. (2019) proposed an indirect flux mapping approach using dual Lambertian targets to reduce interpolation errors in sensor regions [8]. The current methodology closely aligns with such innovative approaches, enhancing spatial resolution and measurement accuracy, thus improving overall flux characterization reliability.

In conclusion, the xenon cinema searchlight-based solar simulator compares favorably with other HFSS configurations in the literature, particularly in terms of peak flux, efficiency, adaptability, and cost-effectiveness. These advantages make it particularly suitable for wide-ranging solar thermal research applications, especially in contexts constrained by budget and space. The results underline substantial potential for further research, development, and optimization of this cinema searchlight-based solar simulator.

Chapter 6: Use Cases - Exemplary Demonstration

The solar simulator was designed to meet the needs of both low-flux and high-flux experimental applications. Each application category imposes distinct performance requirements in terms of irradiance intensity and spatial uniformity. The following sections outline how the simulator was adapted or operated to meet these needs.

Low-flux experiments, such as radiative cooling tests, require irradiance near 1 sun (approximately 1000 W/m²) delivered as uniformly as possible over the test area. To improve spatial uniformity, a ground glass diffuser was placed in front of the lamp output. This diffuser scatters the incident light and produces a more uniform flux distribution across the test area.

High-flux applications, such as thermal decomposition of regolith simulants or high-temperature material testing, demand concentrated irradiance levels capable of driving temperatures above 1000 °C. The simulator achieves peak fluxes reaching 2348 k W/m² under best-focus configurations with the Fresnel lens. Equation x is used to estimate the temperatures expected from this configuration:

$$\alpha q = \varepsilon \sigma T^4 \qquad \text{(eqn.6)}$$

Assuming an absorptivity of α= 0.743, flux q= 2348 k W/m² , emissivity ε = 0.927. The Calculated maximum peak temperature is 2400 K, or 2127 °C. This estimate does not take into account convective and conductive modes of heat transfer.

6.1 Low-Flux Application: Performance Testing of Radiative Cooling Materials

6.1.1 Introduction and Background

The increasing global demand for energy-efficient cooling solutions has intensified interest in passive daytime radiative cooling (PDRC) as a sustainable alternative to conventional air conditioning and refrigeration. Traditional cooling methods rely heavily on electricity, contributing to high energy costs and greenhouse gas emissions. In Canada alone, approximately 6% of total commercial sector energy consumption is dedicated to space cooling, a figure expected to rise as climate change intensifies [20].

PDRC offers an electricity-free cooling mechanism by exploiting the atmospheric transparency window (8–13 μm) to emit thermal radiation into deep space while simultaneously reflecting most

incoming solar radiation [21]. This unique combination enables surfaces to achieve sub-ambient temperatures even under direct sunlight, making PDRC materials highly suitable for building envelopes, electronics, textiles, and industrial thermal management [21].

To be effective, PDRC materials must exhibit high solar reflectivity in the 0.3–2.5μm range to minimize heat gain, while maintaining strong mid-infrared emissivity in the 8–13μm range for heat rejection. Innovations in this field include metamaterials, photonic nanostructures, hierarchical porous polymers, and bioinspired coatings [22–24]. Reported cooling performance varies by location and setup, with sub-ambient temperature reductions ranging from 3.3K in China to 11K in the United States [21]. However, such field tests are subject to inconsistencies in environmental parameters like solar intensity, humidity, and wind speed, which makes material-to-material comparisons unreliable.

To overcome these limitations, standardized indoor testing using solar simulators has gained traction. High-flux solar simulators enable repeatable, controlled evaluation by replicating solar conditions and environmental factors in a laboratory setting. Techniques such as liquid-nitrogen-cooled enclosures for simulating the cold-sky effect and spectral filters to emulate atmospheric transparency allow precise and consistent performance measurements [21]. These controlled conditions are essential for benchmarking new PDRC technologies and guiding their commercial adoption.

This chapter presents the collaborative study between ChillSkyn and York University, which demonstrates the performance of a commercial radiative cooling coating under a controlled, low-flux solar simulation environment. Leveraging the simulator's flexibility and spectral fidelity, this use case enables reliable comparison between coated and uncoated test enclosures. The methodology, experimental setup, and performance analysis detailed in the following sections emphasize the importance of controlled indoor testing in advancing the deployment of passive radiative cooling technologies.

6.1.2 Experimental Setup and Methodology

The experimental setup used in this investigation is shown in Figure 6.1, which provides a detailed SolidWorks CAD model with labeled components. The configuration consists of two electronic enclosures mounted on an optical table (H), creating a controlled environment for thermal

characterization under simulated solar loading. The solar simulator provides an irradiance equivalent to one sun, which is diffused through a ground glass diffuser (A) in order to achieve a more uniform light distribution over the test area. The direction of the incident irradiation is illustrated in the figure by red arrows.

Two enclosures were initially designed to assess the thermal behavior of different surface coatings under identical internal heating conditions. The first enclosure (B) is partially sectioned to allow visualization of its internal components, including two 13 W resistive heaters (E) that generate controlled internal heat loads representative of typical electronic devices. The second enclosure (C) is fully enclosed and features a cap coated with a solar-reflective white paint. In contrast, the first enclosure is equipped with a cap coated with a ChillSkyn Prototype radiative cooling material. This arrangement allows a direct comparison of the thermal performance of different surface treatments under equivalent external and internal thermal conditions.

Cable glands (F) are integrated into the walls of the enclosures to enable the routing of thermocouples and electrical wiring without compromising the thermal insulation. The enclosures are mounted on an 80-20 aluminum extrusion frame (D) to minimize conductive heat transfer to the optical table. In addition, a bottom insulating layer (G) is positioned beneath each enclosure to further reduce heat conduction from the enclosures to the table below.

To simulate radiative heat losses to a cold sky, the assembly is placed within a transparent glass dome (H). The dome is designed to be filled with liquid nitrogen, providing an external environment at approximately –196 °C. The use of the cooled dome enables the experiment to replicate the thermal boundary conditions typically experienced under deep space cold-sky conditions. This allows for a more accurate evaluation of the coatings' thermal performance under real world radiative cooling scenarios.

Following the conceptual design presented in Figure 6.1, the experimental setup was constructed and is shown in Figures 6.2 and 6.3. In the final configuration, a single aluminum enclosure was utilized to ensure consistent experimental conditions throughout all tests. By maintaining a constant enclosure position, heater input, and exposure to incident flux, direct comparisons could be made between different surface treatments. Thermal performance was evaluated by sequentially installing three different caps onto the enclosure: a ChillSkyn Prototype coated cap, a SolarFlex-coated cap, and a bare aluminum cap without any surface coating.

The enclosure was internally heated using resistive heating elements supplying a total power of 16 W, representative of typical low-power electronic devices. Thermocouples were installed to measure surface and internal temperatures, and all data were recorded using a multi-channel data-logger. A regulated power supply maintained constant electrical input to the heaters during each experimental run.

To simulate radiative heat exchange with a cold environment, a dome assembly was positioned around the test area. The dome consisted of a borosilicate glass (Pyrex) kitchen bowl force-fitted into a polyethylene bucket from which the base was removed. A watertight seal between the glass and the polyethylene was achieved using sealing paste. During operation, the dome was continuously filled with liquid nitrogen, with the liquid level maintained just below the flat top surface of the glass bowl.

The dome was installed below the enclosure cap, ensuring that the enclosure was surrounded by a full hemisphere of cold surroundings. This configuration effectively simulated exposure to a cold sky, analogous to radiative cooling to outer space, where temperatures are extremely low. The dome assembly was supported by three aluminum pillars, which ensured proper alignment without making direct contact with the enclosure cap.

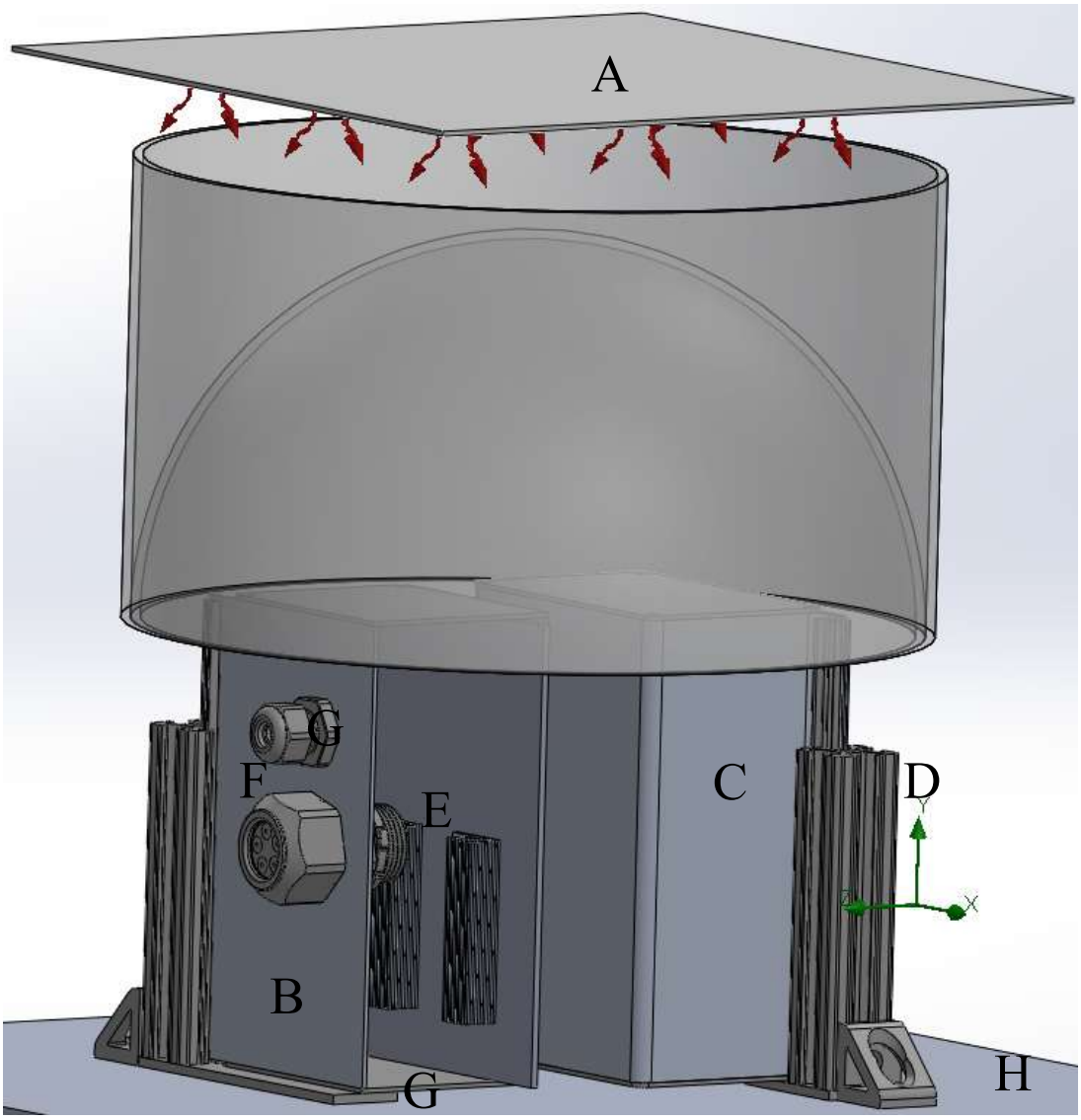

Figure 6.1: SolidWorks model of the experimental setup showing major components used for radiative cooling evaluation under simulated solar radiation.

Figure 6.2 presents a detailed view of the internal configuration of the experimental enclosure. The photograph shows the resistive heaters used to simulate internal heat generation, along with the placement of thermocouples for temperature monitoring. Electrical connections were made using high-temperature wiring and compact wire connectors to ensure reliable and safe operation. A cable gland is mounted on the side of the enclosure to allow external connections. Figure 6.3 shows the setup with the glass dome in place during operation, demonstrating the implementation of the liquid nitrogen-cooled environment.

The constructed experimental setup achieves the intended design objectives, providing a more uniform irradiation, minimizing conductive heat losses, and enabling the evaluation of passive cooling performance under simulated cold sky conditions.

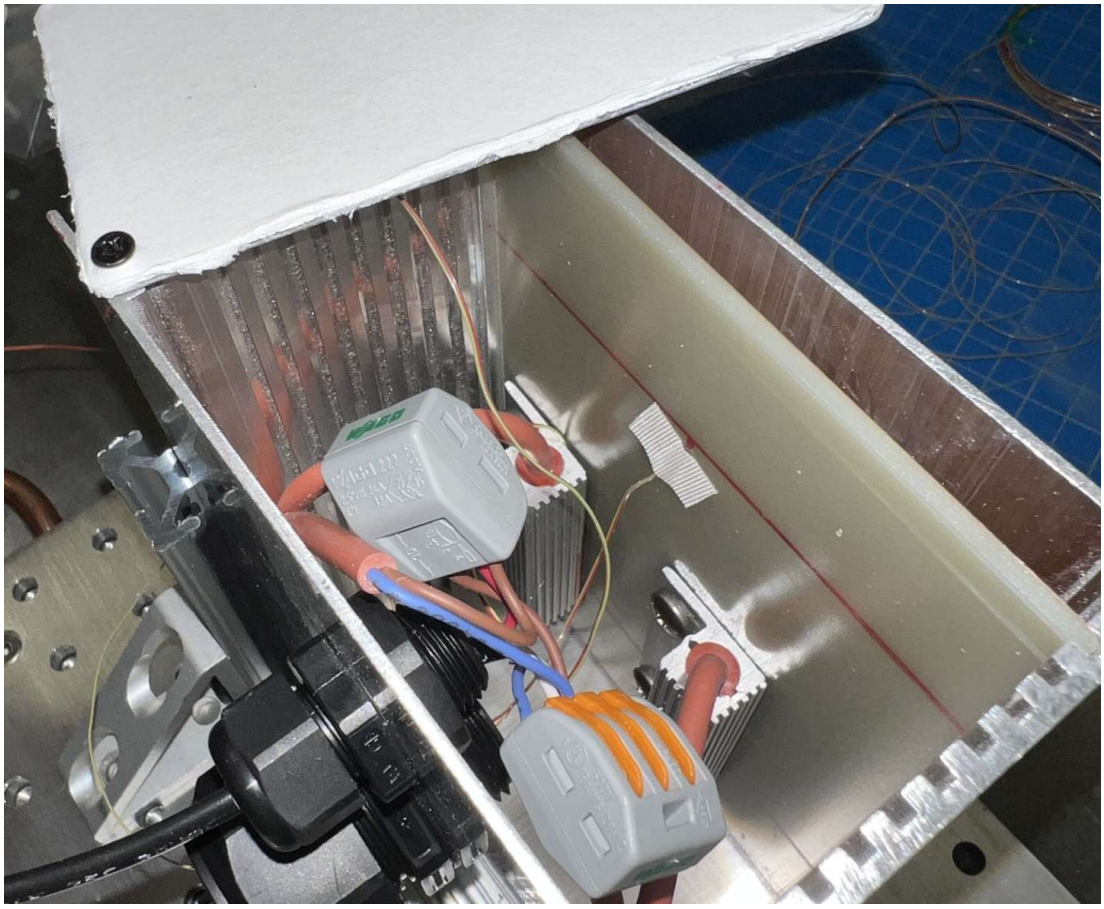

Figure 6.2: Internal view of the experimental enclosure showing the resistive heaters, thermocouples, wiring connections, and cable gland.

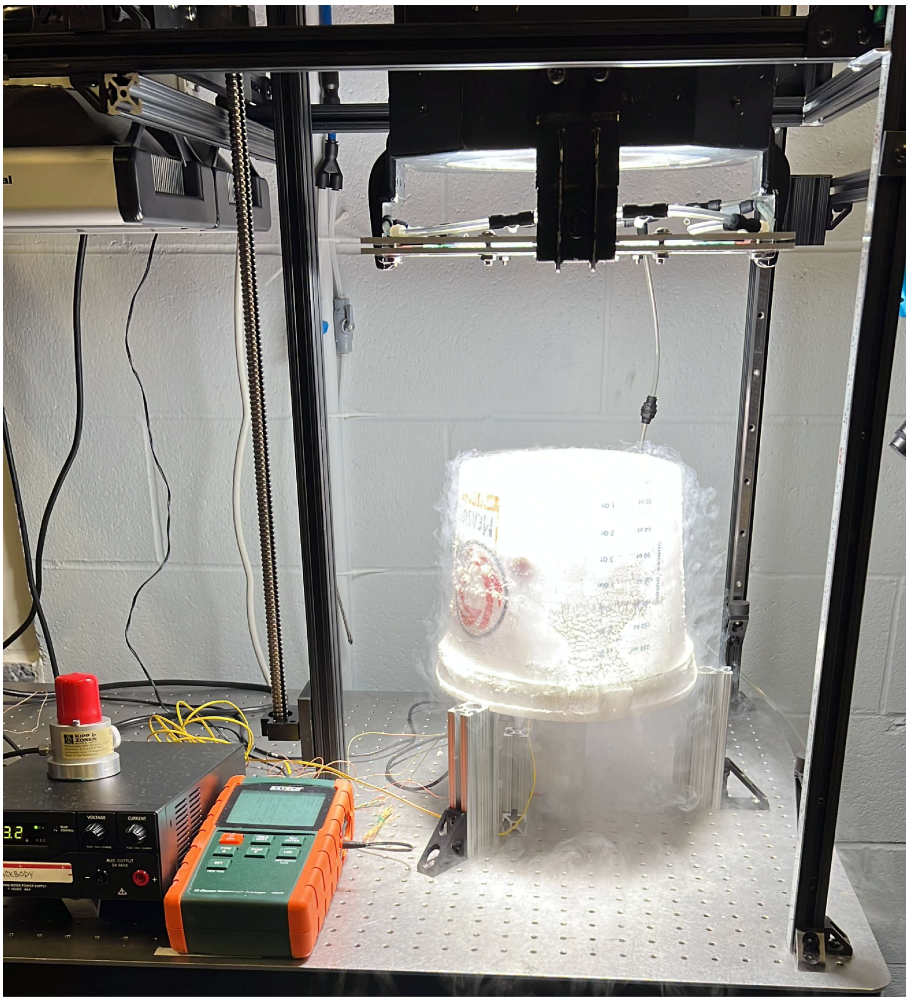

Figure 6.3: Experimental setup showing the aluminum enclosure, power supply, thermocouples, data-logger, and supporting frame mounted on the optical table under the solar simulator. Glass dome is also shown, with vapor visible around the dome.

6.1.3 Results and Discussion

The average steady-state temperatures measured at critical locations within the enclosure are summarized in Table 6.1 for three different cap configurations: bare aluminum, SolarFlex-coated aluminum, and ChillSkyn Prototype coated aluminum. Measurements were recorded at the surface of the heater, the inner surface of the cap, the air inside the enclosure, and the surface of the internal circuit board.

Location	**Bare Aluminum (°C)**	**SolarFlex (°C)**	**ChillSkyn Prototype (°C)**
Heater	90.6	89.1	85.8
Cap underside	16.4	10.2	10.3
Internal air	19.6	15.8	14.1
Circuit board	45.2	44.2	41.6

Table 6.1: Steady-state temperatures measured at the heater, cap, air inside the enclosure, and internal board for different cap surface coatings.

The heater surface temperature is the most critical metric in evaluating the effectiveness of the radiative cooling coatings, as it represents the internal thermal load analogous to real-world components such as battery banks in telecommunications towers or electronics in outdoor enclosures. Reducing the operating temperature of these components directly enhances their efficiency, longevity, and reliability.

The heater temperature showed a clear improvement with the application of radiative cooling coatings, decreasing from 90.6°C with the bare aluminum cap to 89.1°C with SolarFlex and 85.8°C with ChillSkyn Prototype. Although the absolute reductions are modest relative to those observed for the cap or air temperatures, they are highly significant for thermal management of sensitive electronics. Even small decreases in component temperatures can result in substantial increases in lifespan.

The internal board temperatures exhibited a similar trend, decreasing from 45.2°C with the bare aluminum cap to 44.2°C with SolarFlex and 41.6°C with ChillSkyn Prototype. These results further validate the effectiveness of radiative coatings in lowering not only the enclosure's external surfaces but also internal component temperatures.

The cap surface and internal air temperatures demonstrated substantial reductions. The cap temperature decreased from 16.4°C for the bare aluminum surface to 10.2°C and 10.3°C with SolarFlex and ChillSkyn Prototype, respectively. The air inside the enclosure similarly cooled from 19.6°C with the bare aluminum cap to 15.8°C with SolarFlex and 14.1°C with ChillSkyn Prototype. These trends are consistent with the expected performance of passive radiative cooling systems and indicate improved management of thermal loads.

The observed improvements are attributed to the optical properties of the coatings. Both SolarFlex and ChillSkyn Prototype exhibit high solar reflectance, minimizing solar energy absorption. However, ChillSkyn Prototype also possesses a high thermal emittance in the infrared region, enabling more efficient radiative heat loss to the cold surroundings. Consequently, ChillSkyn Prototype consistently achieved the lowest temperatures across all measurement locations. This behavior aligns with the fundamental principles of radiative cooling, where both high reflectance of solar radiation and high infrared emittance are critical for optimal performance.

The use of a liquid nitrogen-cooled dome, maintained at approximately –196°C, provided a stable and idealized radiative sink for the experiment. In real outdoor conditions, surfaces exposed to a cold sky interact radiatively with the cosmic background, which is near 3 K (–270°C). Due to atmospheric transparency in the infrared window (particularly between 8 and 13 μm), surfaces can effectively radiate heat to space. The use of a liquid nitrogen-cooled dome in this study appropriately simulates the radiative cooling potential of a cold sky, providing a conservative and repeatable environment. Although the dome temperature is higher than the cosmic background, it establishes a stable, sub-ambient radiative boundary condition that enables evaluation of the coatings' performance under clear sky scenarios.

It is also important to note that the caps represented only a relatively small fraction of the total surface area of the enclosure. As a result, the full potential of the coatings was underutilized. A larger coated surface area would increase the overall radiative heat loss capacity, thereby further enhancing cooling performance. In the present setup, heat generated by the internal heater was

dissipated primarily through radiation to the surrounding environment, with conduction through the enclosure walls minimized using insulating materials on the aluminum frame supporting the enclosure. Both conductive and convective heat transfer mechanisms were consistent across all experimental runs, as the enclosure configuration, mounting conditions, and ambient environment were identical for each test. Therefore, any variations in internal temperatures can be attributed primarily to differences in radiative behavior associated with the surface coatings since only the cap surfaces were modified.

Overall, these findings demonstrate that passive radiative cooling coatings with both high solar reflectance and high infrared emittance can substantially lower internal component temperatures. The application of such coatings led to measurable reductions in enclosure cap, internal air, and component temperatures, offering a promising passive thermal management strategy for outdoor electronics, satellite enclosures, and extraterrestrial systems where active cooling is impractical.

6.2 High-Flux Application: Conversion of Martian Soil to Oxygen and Structural Metals Using Concentrated Sunlight

6.2.1 Introduction and Motivation

Long-duration human exploration of Mars will require the ability to locally extract essential resources from the Martian environment. Transporting large quantities of oxygen, structural materials, or fuel from Earth is logistically and economically not feasible. As a result, in-situ resource utilization (ISRU) has emerged as a critical enabling technology for sustained off-world habitation.

One promising ISRU pathway is the extraction of oxygen and usable metals from Martian regolith. The surface soil of Mars contains abundant oxides of iron and other metals that can be thermochemically reduced at high temperatures. This process, powered by solar energy, could yield breathable oxygen for life support, metallic products for construction, and process heat for industrial-scale operations [30].

The goal of this study is to explore the feasibility of such a thermochemical reduction process using concentrated artificial sunlight provided by a high-flux solar simulator. By focusing intense solar radiation onto regolith simulant under controlled laboratory conditions, we aim to evaluate both the thermal behavior of the material and the potential for oxygen evolution. This section presents a proof-of-concept demonstration using our focusable solar simulator operating at peak flux conditions.

6.2.2 Background and Theory

Martian regolith is predominantly composed of silicate minerals and iron oxides, making it an abundant source of oxygen and structural materials for future in-situ resource utilization (ISRU) efforts. To support the development of ISRU processes, the JSC Mars-1A regolith simulant, developed by NASA's Johnson Space Center (JSC), is used as a terrestrial analog. This simulant closely matches the mineralogical composition and particle size distribution of native Martian soil, enabling laboratory-scale investigations under controlled conditions [31].

A key thermochemical pathway of interest for oxygen production under Martian conditions involves the sequential reduction of iron (III) oxide (Fe_2O_3) through a series of temperature-dependent reactions:

$$Fe_2O_3\ (s) \rightarrow \frac{2}{3} Fe_3O_4\ (s) + \frac{1}{6} O_2\ (g) \qquad (1200\ K)$$

$$\frac{2}{3}\ Fe_3O_4\ (s) \rightarrow 2\ FeO\ (s) + \frac{1}{3} O_2\ (g) \qquad (2000\ K)$$

$$2\ FeO\ (s) \rightarrow 2\ Fe\ (s) + O_2\ (g) \qquad (3300\ K)$$

These reduction reactions are thermodynamically favorable under the low-pressure and low-oxygen partial pressure conditions characteristic of the Martian atmosphere. However, the specific temperatures listed above correspond to a closed gas system on the Martian surface. In such a system, evolved oxygen gas is trapped during the reaction, resulting in a progressively increasing local oxygen partial pressure that affects the equilibrium temperature thresholds. In open or flowing systems, the reduction steps may proceed at slightly lower temperatures due to continuous removal of oxygen from the reaction zone.

The initial reduction of Fe_2O_3 to magnetite (Fe_3O_4) becomes thermodynamically favorable at temperatures exceeding approximately 1200 K. Higher temperatures are required to drive the further reduction steps toward metallic iron. The evolved oxygen gas can potentially be collected for life support or fuel production, while the resulting metallic phases may serve as structural materials or sintered components.

High-flux solar simulators offer an approach for initiating these thermochemical reactions by concentrating intense radiation onto regolith samples. Compared to conventional furnaces, solar simulators provide rapid, localized heating with excellent spatial control over the irradiated area. By replicating the energetic conditions expected under concentrated Martian sunlight, they enable laboratory-scale feasibility studies of solar-driven ISRU processes.

In the present study, the developed solar simulator was operated in a high-flux configuration to investigate the heating behavior of JSC Mars-1A regolith simulant. Although the maximum temperatures achieved did not exceed the threshold required for complete Fe_2O_3 reduction, the system demonstrated the ability to heat regolith analogs beyond 1250°C under controlled laboratory conditions. This performance validates the capability of the simulator to support early-stage ISRU research by enabling detailed investigation of high-temperature heat and mass transfer phenomena relevant to regolith processing.

6.2.3 Experimental Setup and Methodology

The experimental configuration was designed to investigate the high-temperature heating of Martian regolith simulant using a laboratory-scale, high-flux solar simulator. The solar simulator was operated in its high-power mode with a Fresnel lens attachment installed to concentrate radiation onto a localized target area. The lens height was adjusted so that the focal plane aligned with the top surface of the regolith sample, maximizing flux concentration at the crucible opening.

The regolith simulant, JSC Mars-1A, was contained within a cylindrical crucible fabricated from high-purity aluminum oxide (Al_2O_3). Aluminum oxide was selected for its thermal stability, chemical inertness, and ability to withstand the elevated temperatures anticipated during exposure. The interior of the crucible was lined with high-temperature insulation to minimize radial heat losses and maintain a stable thermal environment for the sample.

JSC Mars-1A simulant was loaded into the crucible, forming a packed bed. A Type K thermocouple was embedded within the regolith, positioned just below the top surface, to monitor the peak temperatures during exposure. The thermocouple was connected to a data logger, which continuously recorded temperature measurements throughout each test.

Visual and thermal diagnostics were employed to characterize the system behavior. A Sony high-speed camera was positioned to record visible changes on the surface of the regolith, capturing any dynamic phenomena such as outgassing, discoloration, or material displacement. Simultaneously, a FLIR thermal infrared camera was aligned with the top surface of the crucible to map the spatial distribution of surface temperatures and identify localized heating effects.

The experimental procedure involved initiating recordings on all diagnostic devices (high-speed camera, thermal camera, and data logger) prior to exposure. Once recording commenced, the solar simulator lamp was gradually lowered, thereby concentrating the light onto the sample until the flux density and surface temperatures peaked. This method allowed for real-time monitoring of the heating process under steadily increasing flux.

Together, this setup enabled controlled high-flux exposure of the regolith simulant under laboratory conditions, allowing for detailed observation of the material's thermal behavior relevant to early-stage ISRU thermal processing.

6.2.4 Results and Discussion

The performance of the solar simulator was evaluated by exposing the JSC Mars-1A regolith simulant to concentrated radiation and observing the thermal and material responses. Thermal camera measurements, shown in Figure 6.4, confirmed that localized peak temperatures of 1286°C were achieved at the sample surface.

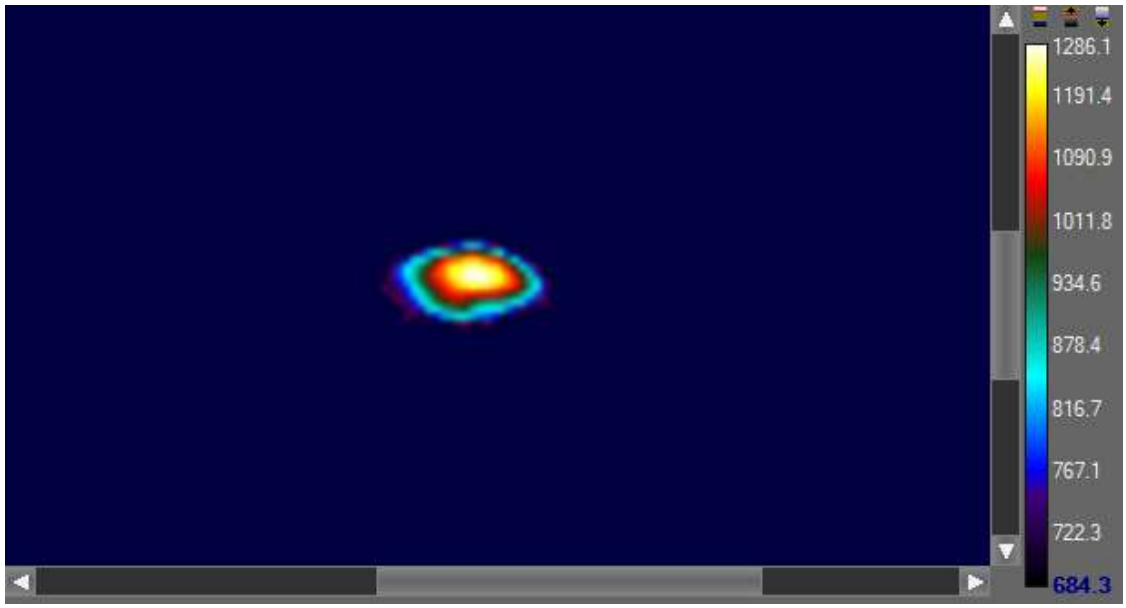

Figure 6.4: Thermal camera image showing localized peak temperatures of approximately 1286°C during high-flux exposure of the regolith simulant.

This temperature is measured with the thermal camera set to an emissivity of 1.00 which does not reflect the actual radiative properties of the surface material. The tested sample consisted of JSC Mars-1A regolith simulant, which has a emissivity of approximately 0.927 [31]. Applying the Stefan–Boltzmann emissivity correction in equation 6:

$$T_{actual} = T_{measured} * (\frac{1.00}{0.927})^{\frac{1}{4}} \quad \text{(eqn.6.2)}$$

The corrected peak temperature becomes approximately 1315.6 °C. This adjusted value more accurately reflects the true thermal state of the surface under concentrated irradiation and is used in subsequent analysis. This temperature falls well below the initial calculated maximum peak achievable temperature of 2127 °C. This is due to the fact that this temperature represents a single

point in isolated space. Neither convection to the surroundings, nor conduction throughout the volume was accounted for in the calculation. For the size comparable to the target area used (20 mm diameter spot size). The average flux is know to be 483 kW/m². Using equation 6, the resulting predicted temperature is of 1343 °C, which much more closely aligned with the experimental temperature achieved.

Although this temperature falls below the threshold required for complete reduction of Fe_2O_3 under Earth's atmospheric conditions, it is sufficient to initiate significant thermal effects such as dehydration, partial sintering, and possible phase transformations within the simulant.

Visual observations recorded by the high-speed camera revealed dynamic behavior at the regolith surface during peak heating. As shown in Figure 6.5, early stages of exposure resulted in localized surface discoloration, with a visible color shift from reddish-brown to a darker hue at the center of the regolith bed. This discoloration is indicative of initial thermal decomposition or dehydration processes within the simulant under increasing flux density.

Figure 6.5: Early stage of thermal exposure showing localized discoloration.

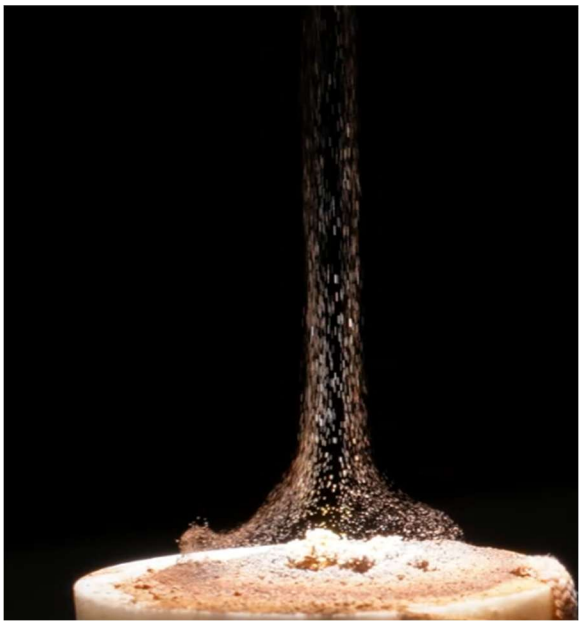

Figure 6.6: Advanced stage of thermal exposure showing vigorous outgassing and material displacement.

As exposure continued, more pronounced thermal effects were observed, as captured in Figure 6.6. Sustained high-flux heating led to vigorous outgassing from the surface, accompanied by dynamic material displacement and localized sintering. A central hotspot formed, characterized by surface melting, darkening, and partial particle fusion. These phenomena suggest progressive thermal degradation and the potential initiation of chemical transformations at regions experiencing the highest temperatures.

Following exposure, the regolith sample was extracted and analyzed. A post-exposure image, shown in Figure 6.7, highlights clear evidence of particle agglomeration and sintering. Several darkened, fused regions are visible within the extracted powder, suggesting localized melting or partial sintering of the regolith particles. These observations are attributed to the peak surface temperatures achieved during exposure. Although full chemical reduction to metallic iron was not attained under the present experimental conditions, the darker coloration and cohesive behavior of the particles suggest the possible formation of lower iron oxides, such as magnetite (Fe_3O_4). Further chemical analysis would be required to confirm the precise nature of these phase transformations.

Figure 6.7: Post-exposure photograph of JSC Mars-1A regolith simulant showing darkened, agglomerated particles indicative of localized sintering and potential phase transformations after high-flux thermal exposure.

The observed thermal and material behaviors are highly relevant to in-situ resource utilization (ISRU) applications. High-temperature sintering of regolith is a critical step for the fabrication of structural materials, such as fabrication of essential habitat components, on extraterrestrial surfaces. Although complete chemical reduction was not realized, the ability of the solar simulator to induce localized high-temperature transformations validates its effectiveness for early-stage ISRU thermal processing experiments.

Overall, the results demonstrate that the developed solar simulator can deliver the high-intensity, spatially localized heating required to drive significant physical changes in regolith simulants. These findings support the use of laboratory-scale solar simulators for the investigation and development of thermal processing strategies applicable to the Moon, Mars, and other planetary bodies.

7. Conclusion

This thesis presented the design, fabrication, and experimental characterization of a novel, low-cost, and adaptable high-flux solar simulator (HFSS) based on commercial xenon arc cinema searchlights. By employing condensing optics such as Fresnel lenses, the developed simulator successfully provided dynamic control over flux intensity, accommodating a wide range of high and low-flux solar thermal applications.

The experimental characterization employed both direct flux measurements with a pyranometer and indirect flux mapping utilizing a CMOS camera. This comprehensive approach enabled precise evaluation of the simulator's irradiance distribution, efficiency, and temporal stability. Key findings demonstrated the simulator's capability to achieve a substantial average irradiance of 2819 W/m² over a 12 × 12-inch target area, and a peak irradiance as high as 2348 kW/m² when combined with a Fresnel lens, highlighting its potential for applications requiring concentrated solar conditions.

Efficiency analyses indicated notable performance improvements at elevated power levels, attaining an efficiency of 22.4% at maximum intensity. Such results underscore the system's potential as a practical and cost-effective alternative to conventional high-flux solar simulators, particularly beneficial for smaller research institutions and industries constrained by financial and infrastructural limitations.

Beyond characterization, the capabilities of the solar simulator were demonstrated through two exemplary applications. In a high-flux application, the simulator was used to heat JSC Mars-1A regolith simulant to peak surface temperatures of 1308°C, initiating partial sintering and thermal transformations relevant to in-situ resource utilization (ISRU) processes for oxygen and structural material extraction on Mars. In a low-flux application, the simulator successfully replicated solar irradiance conditions combined with a liquid nitrogen-cooled dome to simulate a cold sky environment. This setup was used to evaluate the thermal performance of passive radiative cooling coatings, demonstrating measurable temperature reductions in electronics enclosures treated with specialized coatings.

These demonstrations validate the versatility and practical utility of the developed solar simulator, confirming its ability to support a broad range of solar thermal research, from extraterrestrial material processing to sustainable terrestrial cooling technologies. The developed platform lays a solid foundation for further enhancements, including multi-lamp configurations, advanced optical systems, environmental controls, and expanded application areas in both academic research and industrial innovation

Future Work

While the developed solar simulator demonstrated significant capabilities for both high- and low-flux applications, several opportunities exist for further advancement. Future work should focus on improving the optical alignment and flux uniformity of the system to enable more precise and consistent irradiance profiles across larger target areas. Additionally, implementing environmental controls such as vacuum chambers or controlled inert atmospheres would enable more accurate simulation of extraterrestrial conditions, thereby facilitating complete thermochemical reduction reactions during regolith processing experiments.

Further enhancements could include the integration of multi-lamp configurations to achieve even higher flux intensities or the adoption of advanced optical components to improve focusing efficiency. Expanding the range of materials tested under both high-flux and low-flux conditions, including additional passive radiative cooling coatings and extraterrestrial soil simulants, would broaden the application space of the simulator. Finally, long-term thermal cycling studies and durability assessments of materials under repeated solar exposure could provide valuable insights for the design of sustainable infrastructure for future lunar and Martian missions.

References

[1] Ekman, B. M., Brooks, G., & Akbar Rhamdhani, M. (2015). Development of high flux solar simulators for solar thermal research. In *Solar Energy Materials and Solar Cells* (Vol. 141, pp. 436–446). Elsevier B.V. https://doi.org/10.1016/j.solmat.2015.06.016

[2] Sarwar, J., Georgakis, G., LaChance, R., & Ozalp, N. (2014). Description and characterization of an adjustable flux solar simulator for solar thermal, thermochemical and photovoltaic applications. *Solar Energy*, *100*, 179–194. https://doi.org/10.1016/j.solener.2013.12.008

[3] Gallo, A., Marzo, A., Fuentealba, E., & Alonso, E. (2017). High flux solar simulators for concentrated solar thermal research: A review. In Renewable and Sustainable Energy Reviews (Vol. 77, pp. 1385–1402). Elsevier Ltd. https://doi.org/10.1016/j.rser.2017.01.056

[4] Wang, W., Aichmayer, L., Garrido, J., & Laumert, B. (2017). Development of a Fresnel lens based high-flux solar simulator. *Solar Energy*, *144*, 436–444. https://doi.org/10.1016/j.solener.2017.01.050

[5] Li, Q., Wang, J., Qiu, Y., Xu, M., & Wei, X. (2021). A modified indirect flux mapping system for high-flux solar simulators. *Energy*, *235*. https://doi.org/10.1016/j.energy.2021.121311

[6] Xiao, J., Yang, H., Wei, X., & Li, Z. (2019). A novel flux mapping system for high-flux solar simulators based on the indirect method. Solar Energy, 179, 89–98. https://doi.org/10.1016/j.solener.2018.12.034

[7] Mahal, J., Good, P., Ambrosetti, G., & Cooper, T. A. (2022). Contactless thermal mapping of high-temperature solar receivers via narrow-band near-infrared thermography. Solar Energy, 246, 331–342. https://doi.org/10.1016/j.solener.2022.10.004

[8] Gill, R., Bush, E., Haueter, P., & Loutzenhiser, P. (2015). Characterization of a 6 kW high-flux solar simulator with an array of xenon arc lamps capable of concentrations of nearly 5000 suns. *Review of Scientific Instruments*, *86*(12). https://doi.org/10.1063/1.4936976

[9] Damiano Timpano, M. (2022). *DEPLOYABLE VERTICALLY ORIENTED SOLAR COLLECTORS UTILIZING ALL-INFLATED POLYMER CONSTRUCTION*

[10] Dai, S., Chang, Z., Ma, T., Wang, L., & Li, X. (2019). Experimental study on flux mapping for a novel 84 kWe high flux solar simulator. *Applied Thermal Engineering*, *162*. https://doi.org/10.1016/j.applthermaleng.2019.114319

[11] Krueger, K. R., Davidson, J. H., & Lipiński, W. (2011). Design of a new 45 kWe high-flux solar simulator for high-temperature solar thermal and thermochemical research. *Journal of Solar Energy Engineering, Transactions of the ASME*, *133*(1). https://doi.org/10.1115/1.4003298

[12] Teledyne FLIR. (n.d.). Blackfly S BFS-PGE-31S4M GigE camera specifications. Retrieved from https://www.flir.com

[13] Wang, W., Aichmayer, L., Laumert, B., & Fransson, T. (2014). Design and validation of a low-cost high-flux solar simulator using Fresnel lens concentrators. *Energy Procedia*, *49*, 2221–2230. https://doi.org/10.1016/j.egypro.2014.03.235

[14] Zhu, Q., Xuan, Y., Liu, X., Yang, L., Lian, W., & Zhang, J. (2020). A 130 kWe solar simulator with tunable ultra-high flux and characterization using direct multiple lamps mapping. *Applied Energy*, *270*. https://doi.org/10.1016/j.apenergy.2020.115165

[15] Levêque, G., Bader, R., Lipiński, W., & Haussener, S. (2017). High-flux optical systems for solar thermochemistry. *Solar Energy*, *156*, 133–148. https://doi.org/10.1016/j.solener.2017.07.046

[16] Siegel, R., Howell, J.R. (2002). Thermal Radiation Heat Transfer, 4th ed. Taylor & Francis.

[17] WhiteOptics LLC. (n.d.). White98™ - High reflectance white reflector film. Retrieved from https://www.whiteoptics.com

[18] Manzoor, S., Qureshi, S. N., Alsharif, M. H., Rana, A., Naqvi, M., & Al-Sulaiman, F. A. (2024). A comprehensive review of state-of-the-art concentrating solar power (CSP). Energy Reports, 10, 3537–3564. https://doi.org/10.1016/j.egyr.2024.02.095

[19] Ho, C. K., and Khalsa, S. S. (July 5, 2012). "A Photographic Flux Mapping Method for Concentrating Solar Collectors and Receivers." ASME. J. Sol. Energy Eng. November 2012; 134(4): 041004. https://doi.org/10.1115/1.4006892.

[20] Thomas Cooper, Proposal_Template-Alliance_Grants_e_York_ChillSkyn_v9.pdf

[21] Song, Q., Tran, T., Herrmann, K., Lauster, T., Breitenbach, M., & Retsch, M. (2022). A tailored indoor setup for reproducible passive daytime cooling characterization. *Cell Reports Physical Science*, *3*(8). https://doi.org/10.1016/j.xcrp.2022.100986

[22] Mandal, J., Fu, Y., Overvig, A. C., Jia, M., Sun, K., Shi, N. N., Zhou, H., Xiao, X., Yu, N., & Yang, Y. (2018). Hierarchically porous polymer coatings for highly efficient passive daytime radiative cooling. Science, 362(6412), 315–319. https://doi.org/10.1126/science.aat9513

[23] Wang, T., Wu, Y., Shi, L., Hu, X., Chen, M., & Wu, L. (2021). A structural polymer for highly efficient all-day passive radiative cooling. Nature Communications, 12, 365. https://doi.org/10.1038/s41467-020-20646-7

[24] Li, X., Peoples, J., Huang, Z., Zhao, Z., Qiu, J., & Ruan, X. (2020). Full daytime sub-ambient radiative cooling in commercial-like paints with high figure of merit. Cell Reports Physical Science, 1(11), 100221. https://doi.org/10.1016/j.xcrp.2020.100221

[25] Project source: ChillSkyn, 20250130-yorku-enclosure-project

[26] Zhai, Y., Ma, Y., David, S. N., Zhao, D., Lou, R., Tan, G., Yang, R., & Yin, X. (2017). Scalable-manufactured randomized glass-polymer hybrid metamaterial for daytime radiative cooling. Science, 355(6329), 1062–1066. https://doi.org/10.1126/science.aai7899

[27] Rephaeli, E., Raman, A., & Fan, S. (2013). Ultrabroadband photonic structures to achieve high-performance daytime radiative cooling. Nano Letters, 13(4), 1457–1461. https://doi.org/10.1021/nl4004283

[28] Shi, N. N., Tsai, C. C., Camino, F., Bernard, G. D., Yu, N., & Wehner, R. (2015). Keeping cool: Enhanced optical reflection and radiative heat dissipation in Saharan silver ants. Science, 349(6245), 298–301. https://doi.org/10.1126/science.aab3564

[29] Wang, X., Liu, X. H., Li, Z. Y., Zhang, H. W., Yang, Z. W., Zhou, H., & Fan, T. X. (2020). Scalable flexible hybrid membranes with photonic structures for daytime radiative cooling. Advanced Functional Materials, 30, 1907562. https://doi.org/10.1002/adfm.201907562

[30] Appelbaum, J., & Flood, D. J. (1989). *Solar Radiation on Mars*.

[31] Salisbury, J. W., & D'Aria, D. M. (2010). Infrared (2.1–25 μm) remote sensing of soil particle size. NASA Technical Memorandum NASA/TM-2010-216738. https://ntrs.nasa.gov/api/citations/20100033114/downloads/20100033114.pdf

[32] Gallo, A., Marzo, A., Fuentealba, E., & Alonso, E. (2017). *High flux solar simulators for concentrated solar thermal research: A review*. **Renewable and Sustainable Energy Reviews**, 77, 1385–1402. https://doi.org/10.1016/j.rser.2017.01.056

[33] Nakar, D., Malul, A., Feuermann, D., & Gordon, J. M. (2008). *Radiometric characterization of ultrahigh radiance xenon short-arc discharge lamps*. **Applied Optics**, 47(2), 224–229. https://doi.org/10.1364/AO.47.000224